

# How eigenmode self-interaction affects zonal flows and convergence of tokamak core turbulence with toroidal system size

Ajay C.J.<sup>1†</sup>, Stephan Brunner<sup>1</sup>, Ben McMillan<sup>2</sup>, Justin Ball<sup>1</sup>, Julien Dominski<sup>3</sup>, and Gabriele Merlo<sup>4</sup>

<sup>1</sup>Ecole Polytechnique Fédérale de Lausanne (EPFL), Swiss Plasma Center, CH-1015 Lausanne, Switzerland

<sup>2</sup>Centre for Fusion, Space and Astrophysics, Department of Physics, University of Warwick, CV4 7AL, Coventry, UK

<sup>3</sup>Princeton Plasma Physics Laboratory, Princeton University, P.O. Box 451, Princeton, New Jersey 08543-0451, USA

<sup>4</sup>The University of Texas at Austin, Austin, Texas 78712, USA

(Received xx; revised xx; accepted xx)

Self-interaction is the process by which a microinstability eigenmode that is extended along the direction parallel to the magnetic field interacts non-linearly with itself. This effect is particularly significant in gyrokinetic simulations accounting for kinetic passing electron dynamics and is known to generate *stationary*  $E \times B$  zonal flow shear layers at radial locations near low order mode rational surfaces (Weikl *et al.* 2018). We find that self-interaction in fact plays a very significant role in also generating *fluctuating* zonal flows, which is critical to regulating turbulent transport *throughout* the radial extent. Unlike the usual picture of zonal flow drive in which microinstability eigenmodes coherently amplify the flow via modulational instabilities, the self-interaction drive of zonal flows from these eigenmodes are uncorrelated with each other. It is shown that the associated shearing rate of the fluctuating zonal flows therefore reduces as more toroidal modes are resolved in the simulation. In simulations accounting for the full toroidal domain, such an increase in the density of toroidal modes corresponds to an increase in the toroidal system size, leading to a finite system size effect that is distinct from the well-known profile shearing effect.

## 1. Introduction

Microturbulence driven by small Larmor-scale instabilities is in most cases the dominant cause of heat and particle loss from the core of magnetic confinement fusion devices and therefore presents a major challenge in achieving burning plasma conditions (Horton 1999). The role of passing electron dynamics in turbulent transport driven by ion-scale microinstabilities, in particular Ion Temperature Gradient (ITG) and Trapped Electron Mode (TEM) instabilities, has been given relatively little attention. In first approximation, these particles, which are highly mobile along the confining magnetic field, are assumed to respond adiabatically to the low frequency ion-scale modes. However, in a tokamak geometry, the phase velocity parallel to the magnetic field of a perturbation with fixed mode numbers  $m$  and  $n$  in the poloidal and toroidal directions, respectively, becomes infinite at the radial position  $r_{m,n}$  of the corresponding Mode Rational Surface (MRS), where the magnetic safety factor profile  $q_s(r)$  is such that  $q_s(r_{m,n}) = m/n$ . Consequently,

† Email address for correspondence: [ajay.chandrarajanjayalekshmi@epfl.ch](mailto:ajay.chandrarajanjayalekshmi@epfl.ch)

at these positions, the condition for passing electrons to respond adiabatically gets violated and their non-adiabatic response becomes important. One notes that, given the toroidal axisymmetry of a tokamak, each linear microturbulence eigenmode has a fixed toroidal mode number  $n$ , but is in general a superposition of many poloidal Fourier modes  $m$ , so that associated MRSs are the positions  $r_{m,n}$  for the different values of  $m$ .

In fact, as a result of the non-adiabatic passing electron dynamics, linear ITG and TEM eigenmodes can become significantly extended along the magnetic field lines (Hallatschek & Dorland 2005), producing fine radial structures at corresponding MRSs (Falchetto *et al.* 2003; Chowdhury *et al.* 2008). These fine structures on the eigenmodes persist in corresponding turbulence simulations, and via non-linear couplings lead to stationary corrugations on the radial profiles of density, temperature and in particular  $E \times B$  zonal shear flows, aligned with low order MRSs, which effectively appear as fine-scale transport barriers (Waltz *et al.* 2006; Dominski *et al.* 2015, 2017). Given that shearing and decorrelation of turbulent eddies by zonal flows is a primary mechanism by which turbulence saturates (Biglari *et al.* 1990; Waltz *et al.* 1994; Rosenbluth & Hinton 1998; Lin *et al.* 1998), it is clearly of interest to understand the generation of these fine scale zonal flow structures in detail.

The generation of the fine zonal flow structures at low order MRSs, via a process called self-interaction, has in fact already been discussed to some length in the work by Weikl *et al.* (2018). The general motivation for the work presented in this paper has been to further investigate the properties of zonal flow drive from this self-interaction mechanism. This process essentially involves each individual microturbulence eigenmode interacting non-linearly with itself to produce a Reynolds stress contribution to the zonal flow drive, which turns out to be located around its corresponding MRSs. Key to this self-interaction is the fact that an eigenmode which is significantly extended along the magnetic field line ‘bites its tail’ after one poloidal turn. For each eigenmode, self-interaction will therefore be particularly significant at its MRSs, given that the radially fine structures located at these positions, resulting from the non-adiabatic passing electron response, are elongated along the magnetic field lines. At low order MRSs (in practice implying mainly integer and half-integer  $q_s$ -surfaces), these self-interaction contributions to Reynolds stress from the different eigenmodes radially align and add up constructively to drive the stationary  $E \times B$  zonal shear flows. Clear illustrations of these fine stationary zonal flow structures can be seen for example in figure 2 of Ref. (Waltz *et al.* 2006), figure 12 of Ref. (Dominski *et al.* 2017), figure 3 of Ref. (Weikl *et al.* 2018), and figure 4 of this paper.

It is important to point out that in the core of a tokamak, low order MRSs are in fact few and far apart, whereas the radial domains between them occupy the majority of the plasma volume. Therefore, at least as important as understanding how self-interaction generates the above-mentioned stationary structures at lowest order MRSs, clearly visible on any flux surface-averaged field, is to address how the same self-interaction mechanism might affect zonal flow drive and therefore turbulent transport in the radial regions *between* low order MRSs. Addressing this question is the main focus of this paper.

While lowest order MRSs are common to all eigenmodes, between them, the MRSs related to the various microturbulence modes tend to be radially misaligned. Hence, in these radial regions, the self-interaction contributions to Reynolds stress from these modes tend to cancel each other out when averaged over time, thus resulting in a nearly *zero stationary* component of the zonal flows. But, given that in the turbulent phase amplitudes of the various microinstability eigenmodes vary in time and furthermore are decorrelated with each other, this cancellation is not ensured at each time instant but only on average over time. As a result, self-interaction drives a *non-zero fluctuating* zonal flow component between low order MRSs.

An important observation resulting from our study is that in simulations accounting for non-adiabatic passing electron dynamics, self-interaction contributions to Reynolds stress from the various microturbulence modes can indeed be significant in the radial regions between lowest order MRSs and in fact act as *random decorrelated kicks* that can in some cases actually disrupt what is usually considered the main drive mechanism of zonal flows - modulational instability (Hasegawa & Mima 1978; Hasegawa *et al.* 1979; Chen *et al.* 2000). The modulational instability mechanism involves the resonant decays of microinstability modes into zonal modes via secondary microinstability daughter modes. Unlike self-interaction, it is a *coherent* process, leading to a *correlated* contribution from the various microinstability modes to the Reynolds stress drive of zonal modes.

In order to quantify the relative importance of the two alternative, possibly competing mechanisms driving zonal flows, *i.e.* self-interaction and modulational instability, we have studied the statistical properties of the Reynolds stress contributions from the various microturbulence modes. Given the different nature of the two driving processes, one can identify high correlation levels between the mode contributions to conditions where modulational instability drive dominates, while lower correlation levels are characteristic of a significant effect from self-interaction. Central to this statistical analysis has been a series of gyrokinetic simulations obtained for identical driving conditions but varying the number of significant toroidal modes participating in the turbulence. Varying the number of toroidal modes changes in particular the number of associated random kicks from self-interaction to the zonal flow drive at each radial position.

Varying the number of significant toroidal modes is in fact related to varying the system size, typically measured by  $\rho^* = \rho_i/a$ , *i.e.* the ratio of the thermal ion Larmor radius  $\rho_i$  to the minor radius  $a$  of the tokamak. Indeed, invoking the fact that the unstable modes driving ion-scale microturbulence are such that  $k_\perp \rho_i \lesssim 1$ , where  $k_\perp$  is the wave vector component perpendicular to the magnetic field, and furthermore noticing that for a given eigenmode with toroidal mode number  $n$  an estimate for  $k_\perp$  is given by the poloidal wave vector component, which in turn can be evaluated as  $k_\chi \simeq m/r_0 \simeq nq_s(r_0)/r_0$  [ $r_0$  is the average radial position of the eigenmode and  $m$  its characteristic poloidal mode number estimated as  $m \simeq nq_s(r_0)$ , given that fluctuations are nearly field-aligned], one obtains that  $k_\perp \rho_i \simeq nq_s(r_0)\rho_i/r_0 = (q_s a/r_0)n\rho^* \sim n\rho^*$ , so that the number  $N_\varphi$  of toroidal modes contributing to the turbulence scales as  $N_\varphi \sim 1/\rho^*$ .

In view of what has just been said, it may at first sight appear surprising that the study presented in this paper is in fact based on simulations carried out in the framework of the flux-tube model (Beer *et al.* 1995), whose underlying assumption is the scale separation between the characteristic length of microturbulence ( $\sim$  Larmor radius  $\rho$ ) and the characteristic length of equilibrium ( $\sim$  minor radius  $a$ ), hence *a priori* achieved by taking the strict limit  $\rho^* \rightarrow 0$  of the gyrokinetic equations. In this limit, the radial dependence of all equilibrium profiles and their gradients appearing in the gyrokinetic equations are constant over the flux-tube volume. There is however one exception to this in the standard flux tube model (Scott 1998): a linearized radial dependence of the safety factor profile  $q_s(r)$  ( $\sim$  constant magnetic shear approximation) is kept in the twist and shift boundary condition applied after usually following the magnetic field line a single turn in the poloidal direction. Through this parallel boundary condition, an eigenmode 'bites its tail' and in particular correctly accounts for the possible resonances that may develop at its associated MRSs. The fact that the eigenmodes correctly "feel" their associated MRSs is obviously key to the development of the fine radial structures and related non-linear self-interaction which is the focus of our study. Also, close agreement between flux-tube (Dominski *et al.* 2015) and global (Dominski *et al.* 2017) gyrokinetic simulations regarding the characteristics of the fine stationary zonal flow structures at

lowest order MRSs clearly confirm that the dynamics of the self-interaction mechanism can indeed be correctly accounted for using such a local model.

Let us already briefly provide here some further insight into how the toroidal spectral density is varied in a flux-tube code (all details will be given in §2). The flux-tube version of the GENE code (Jenko *et al.* 2000; Merz 2008) which we have applied for the present study, considers the field aligned coordinate system defined [in equations (2.1-2.3)] by the variables  $(x, y, z)$  which are respectively the radial, binormal and parallel coordinates. Note that the binormal coordinate  $y$  is the only one of the three coordinates  $(x, y, z)$  which actually depends on the toroidal angle  $\varphi$ . The length  $L_y$  of the flux-tube in this direction can thus be associated to its angular extent  $\Delta\varphi$  along  $\varphi$ :  $L_y = C_y \Delta\varphi$ , where the constant  $C_y = r_0/q_0$  ensures that  $y$  has units of length,  $r_0$  being the radial position at which the flux-tube is positioned and  $q_0 = q_s(r_0)$ . Also, as a linear eigenmode has a fixed toroidal mode number  $n$ , it consequently has a fixed Fourier mode number  $k_y$  with respect to  $y$  when represented in field-aligned coordinates, given by  $k_y = n/C_y = nq_0/r_0$ , *i.e.*  $k_y$  is actually equivalent to the previously mentioned poloidal mode number estimate  $k_\chi$ . The significant  $k_y$  modes contributing to ion-scale turbulence are therefore such that  $k_y \rho_i \lesssim 1$ , and given that the minimum mode number for a flux-tube box with length  $L_y$  is given by  $k_{y,\min} = 2\pi/L_y$ , the number of toroidal modes contributing to the turbulence is estimated as  $N_\varphi \simeq 1/k_{y,\min} \rho_i = (1/2\pi)L_y/\rho_i$ . Hence, when studying microturbulence using flux-tube simulations, carrying out a scan in  $k_{y,\min} \rho_i$  (or equivalently  $L_y/\rho_i$ ) corresponds to varying the toroidal spectral density.

In view of the above, it is therefore possible to realistically study the importance of the self-interaction mechanism via a flux-tube simulation for a given size tokamak, characterized by a finite  $\rho^*$  value, by considering the appropriate toroidal spectral density, *i.e.* by setting  $k_{y,\min} \rho_i = \rho_i/C_y = (q_0 a/r_0) \rho^*$  corresponding to the toroidal mode number  $n = 1$  (one naturally recovers here that the number of modes contributing to turbulence scales as  $N_\varphi \simeq 1/k_{y,\min} \rho_i \sim 1/\rho^*$ ). This is clearly equivalent to setting  $L_y = 2\pi C_y$ , *i.e.*  $\Delta\varphi = 2\pi$ , which along with parallel box length  $L_z = 2\pi$  implies having the flux-tube cover the *full* magnetic surface once. Therefore, considering a finite  $k_{y,\min} \rho_i$  value in a flux-tube simulation effectively corresponds to accounting for a finite  $\rho^*$  effect. All other finite  $\rho^*$  effects such as profile shearing (Waltz *et al.* 1998, 2002), or finite radial extent of the unstable region (McMillan *et al.* 2010), are however obviously absent in a flux-tube.

Given that  $k_{y,\min} \rho_i \sim \rho^*$ , the true flux-tube model would require considering the limit of  $k_{y,\min} \rho_i \rightarrow 0$ . In numerical simulations however, for obvious practical reasons,  $k_{y,\min} \rho_i \sim \rho_i/L_y$  is always finite, so that if turbulence actually converges for  $k_{y,\min} \rho_i \rightarrow 0$ , this limit can at best be approximately approached in the limit of large box length  $L_y/\rho_i$ , which may become numerically prohibitive. Thus, carrying out the above mentioned  $k_{y,\min} \rho_i$  scan also enables us to investigate whether/how the flux-tube simulation results converge as  $k_{y,\min} \rho_i \rightarrow 0$ , a problem that was already addressed in our sister paper (Ball *et al.* 2020). It is remarkable that, to our knowledge, the convergence of flux-tube gyrokinetic turbulence simulations with respect to  $k_{y,\min} \rho_i$  seems not to have been given more attention in the literature, at least not considering fully kinetic electron dynamics. Our simulations of ITG-driven turbulence indeed illustrate that for practical values of  $k_{y,\min} \rho_i$ , typically chosen in the range  $10^{-2} - 10^{-1}$ , convergence of turbulent fluxes is in many cases not yet reached. Particularly in the case of strong background temperature gradients, *i.e.* away from marginal stability, the gyro-Bohm normalised ion heat flux  $Q_i$  keeps on increasing with a nearly algebraic scaling  $Q_i \sim (k_{y,\min} \rho_i)^\alpha$ ,  $\alpha > 0$ , when decreasing  $k_{y,\min} \rho_i$ , thus showing no apparent sign of convergence within this range of values. In the particular strong gradient case considered, corresponding to parameters near to the Cyclone Base Case (CBC) (Dimitis *et al.* 2000), one has

$\alpha \simeq 0.45$  (see Fig. 7 in this paper), so that  $Q_i$  increases by nearly a factor of 3 over the range  $k_{y,\min}\rho_i = 10^{-2} - 10^{-1}$ . In agreement with related work by one of our co-authors (Ball *et al.* 2020), for sufficiently small values of  $k_{y,\min}\rho_i$ , the algebraic scaling is ultimately broken and convergence of the fluxes is finally approached within  $\sim 5\%$  for  $k_{y,\min}\rho_i \simeq 5 \cdot 10^{-3}$  (see Fig. 18). But this corresponds to a value of  $k_{y,\min}\rho_i$  one order of magnitude smaller than usually considered. For gradients closer to marginal stability, this dependence of  $Q_i$  on  $k_{y,\min}\rho_i$  appears to be weakened and convergence approached already for somewhat larger, numerically more affordable values. This can be seen as good news, as gradients near marginal stability may be considered as the physically most relevant cases. It nonetheless appears essential that one keeps in mind this potentially significant dependence of the fluxes on  $k_{y,\min}\rho_i$  in the range of typically considered values, which seems to have very often been overlooked or at least not been given sufficient attention in past studies.

In conjunction with the observed increase in fluxes with system size over the considered range of  $k_{y,\min}\rho_i = 10^{-2} - 10^{-1}$ , a decrease in the shearing rate associated to fluctuating zonal flows is also observed [see Fig. 6(c)]. Via a simple “back-of-the-envelope” estimate, this decrease in the shearing rate associated to fluctuating zonal flows is shown to result from the fact that the self-interaction drive of zonal flows from the various microturbulence modes are decorrelated with each other.

The remainder of this paper is organized as follows.

Important aspects of the flux-tube version of the grid-based gyrokinetic code GENE (Jenko *et al.* 2000; Merz 2008; Görler *et al.* 2011), which was used for performing the simulations in this study, are presented in §2. Details of its field-aligned coordinate system are recalled, in particular how the parallel boundary conditions ensure that linear eigenmodes correctly “feel” associated MRSs.

A brief summary of a set of previous studies (Dominski *et al.* 2015, 2017), addressing the role of non-adiabatic passing electron dynamics and which provided the starting point for the main work presented in this paper, is given in §3. The same ITG-driven turbulence case as in (Dominski *et al.* 2015) will in fact also be considered as a reference case here. Its parameters are recalled as well as the linear frequency and growth rate spectra. Also pointed out are the fine radial structures that develop on the linear eigenmodes as a result of the non-adiabatic passing electron dynamics. Furthermore summarized is how these fine structures on the eigenmodes act as channels for electron heat and particle transport, and, through non-linear coupling, are observed to lead to corrugations at low order MRSs of the time-averaged density and temperature profiles as well as  $E \times B$  zonal flow shear layers.

The main results for the present study, consisting of non-linear flux-tube simulations of ITG-driven turbulence are presented in §4. Sets of simulations have been obtained by scanning  $k_{y,\min}\rho_i$  over the typical range of values considered in practice, *i.e.*  $k_{y,\min}\rho_i = 10^{-2} - 10^{-1}$ . These scans were repeated considering ion temperature gradients both near and far from marginal stability. Furthermore, to clearly illustrate how the fine radial structures resulting from the non-adiabatic passing electron dynamics lead to particularly strong contributions to zonal flow drive from the self-interaction mechanism, simulations with two different electron models were carried out: either considering fully kinetic electron dynamics or enforcing their fully adiabatic response (fine radial structures being absent with the latter model). First analysis of results are carried out in this same section, showing that especially in the case of fully kinetic electrons and far from marginal stability, heat fluxes  $Q_i$  have not yet converged over the considered range of typical  $k_{y,\min}\rho_i$  values. Given its key role in saturating ITG-driven turbulence, the level of zonal flow shearing rate,  $\omega_{E \times B}$ , is carefully diagnosed. It is shown how in all cases

this shearing rate decreases with decreasing  $k_{y,\min}\rho_i$  (see figure 6). Also analyzed is the radial correlation length of the turbulence. An important observation is that for sufficiently small  $k_{y,\min}\rho_i$ , the radial extent of turbulent eddies presents a clearly shorter scale length than the distance between lowest order MRSs (figure 8). From this one concludes that, for these lower values of  $k_{y,\min}\rho_i$ , the turbulence is mostly sheared by the zonal flows between lowest order MRSs, where  $\omega_{E\times B}$  is essentially composed of its fluctuating component, rather than sheared by the stationary component of  $\omega_{E\times B}$  located at the lowest order MRSs.

Section 5 is dedicated to understanding why fluctuating zonal shear flow level decreases with  $k_{y,\min}\rho_i$ . To this end, the different zonal flow driving mechanisms are analyzed in detail. After showing in §5.1 that Reynolds stress can be considered as a proxy for measuring the drive of zonal flows, we review the two basic zonal flow driving mechanisms: modulational instability in §5.2 and self-interaction in §5.3. To illustrate these two basic mechanisms, reduced non-linear simulations are presented in §5.4, where the drive of zonal modes via the decay of an initially single finite amplitude ITG eigenmode is studied. These simulations are carried out with both adiabatic and kinetic electrons to demonstrate the dominant role of modulational instability in the former case and the significant role of self-interaction in the latter.

Evidence of the self-interaction and the modulational instability mechanisms in fully developed turbulence is then addressed in §5.5 and §5.6, respectively. A comparison between simulations with adiabatic and kinetic electrons is done here as well. It is shown that the self-interaction mechanism is persistent in the turbulence simulations accounting for fully kinetic electrons, while it is weak in simulations with adiabatic electrons, consistent with the reduced nonlinear simulations. Using statistical methods such as bicoherence and Reynolds stress correlation analysis diagnostics, we show that the self-interaction contributions to Reynolds stress from the various microturbulence modes are decorrelated in time, and essentially act as random kicks on the zonal modes, while the contributions from modulational instability, which is a coherent process, are correlated with each other. In the case of adiabatic electron simulations, strong correlation between Reynolds stress contributions from different modes as well as large bicoherence levels are measured, reflecting that self-interaction is indeed weak and zonal flow drive is dominated by the modulational instability. In the case of kinetic electrons however, self-interaction may disrupt the zonal flow drive from modulational instability and, consequently, correlation between Reynolds stress contributions as well as bicoherence levels are found to be relatively weak (see figures 15 and 16).

Based on the study carried out in §5, providing evidence of the decorrelated nature of the self-interaction contributions to zonal flow drive from the various microturbulence modes, we carry out a “back-of-the-envelope” derivation, using simple statistical arguments, to predict the scaling observed in simulations with kinetic electrons of the zonal flow shearing rate  $\omega_{E\times B}$  with  $k_{y,\min}\rho_i$ . This derivation is presented in §6.

Final discussion and conclusions are provided in §4 7.

## 2. The GENE flux-tube model

GENE is an Eulerian electromagnetic gyrokinetic code. The flux-tube version of the code is used in this study. In view of the issues addressed in this paper, we recall some important features of the flux-tube model (scaling assumptions, field-aligned coordinate system, boundary conditions).

GENE uses a non-orthogonal, field-aligned coordinate system  $(x, y, z)$  defined in terms

of the magnetic coordinates  $(\psi, \chi, \varphi)$  as follows (Beer *et al.* 1995) :

$$x = x(\psi) \quad : \text{radial coordinate}, \quad (2.1)$$

$$y = C_y[q_s(\psi)\chi - \varphi] \quad : \text{binormal coordinate}, \quad (2.2)$$

$$z = \chi \quad : \text{parallel coordinate}. \quad (2.3)$$

$\psi, \chi$  and  $\varphi$  represent the poloidal magnetic flux, straight field line poloidal angle and the toroidal angle respectively. The function  $x(\psi)$  is a function of  $\psi$  with units of length.  $C_y = r_0/q_0$  is a constant, where  $q_0$  is the safety factor at  $r_0$  denoting the radial position of the flux-tube. The inverse aspect ratio of the flux-tube is defined as  $\epsilon = r_0/R$ , where  $R$  is the major radius of the tokamak.

The flux-tube model assumes a scale separation between the radial correlation length of turbulent eddies ( $\sim \rho_i$ ) and the radial length scale of variation of equilibrium ( $\sim a$ ), thus corresponding to the limit  $\rho^* = \rho_i/a \ll 1$ . Consistent with this scale separation, the background density and temperature gradients, as well as the magnetic equilibrium quantities, are considered constant across the radial extension  $L_x$  of the flux-tube, and are evaluated at  $r_0$ . An exception is the safety factor appearing in the parallel boundary condition, discussed in detail later in this section. The background density and temperature of a species  $j$  are, respectively,  $N_{j,0} = N_{j,0}(r_0)$  and  $T_{j,0} = T_{j,0}(r_0)$  and their inverse radial gradients lengths are  $1/L_{Nj} = -d \log N_{j,0}/dr|_{r=r_0}$  and  $1/L_{Tj} = -d \log T_{j,0}/dr|_{r=r_0}$ . The magnetic field amplitude  $B_0 = B_0(z)$ , Jacobian  $\mathcal{J}^{xyz} = \mathcal{J}^{xyz}(z)$  and the metric coefficients  $g^{\mu\nu}(z) = \nabla\mu \cdot \nabla\nu$  where  $\mu$  and  $\nu$  are the flux-tube coordinates  $(x, y, z)$ , depend only on the parallel coordinate.

The flux-tube coordinates  $(x, y, z)$  satisfy the double periodic boundary condition in a tokamak as follows. The  $\Delta\varphi$ -periodicity of any physical quantity  $\mathcal{A}$ , in particular fluctuations, along the toroidal direction  $\varphi$  reads:

$$\mathcal{A}(\psi, \chi, \varphi + \Delta\varphi) = \mathcal{A}(\psi, \chi, \varphi),$$

and translates in  $(x, y, z)$  coordinates to an  $L_y$ -periodicity along  $y$ :

$$\mathcal{A}(x, y + L_y, z) = \mathcal{A}(x, y, z). \quad (2.4)$$

where  $L_y = C_y \Delta\varphi$ . If the flux-tube covers the full flux-surface,  $\Delta\varphi = 2\pi$ , else  $\Delta\varphi$  is only a fraction of  $2\pi$ . The  $2\pi$ -periodicity in the poloidal direction  $\chi$  reads:

$$\mathcal{A}(\psi, \chi + 2\pi, \varphi) = \mathcal{A}(\psi, \chi, \varphi),$$

and translates in  $(x, y, z)$  coordinates to a pseudo-periodic condition along  $z$ :

$$\mathcal{A}(x, y + C_y q_s(x) 2\pi, z + 2\pi) = \mathcal{A}(x, y, z). \quad (2.5)$$

This boundary condition is referred to as the parallel boundary condition (Scott 1998). Note that in the flux-tube model in general, one can consider a periodicity in  $z$  that is larger than  $2\pi$  as well (Beer *et al.* 1995; Faber *et al.* 2018; Ball *et al.* 2020). However, typically the  $2\pi$ -periodicity is considered, as it is in this work.

Furthermore, the radial scale separation  $\rho^* \ll 1$  justifies periodic boundary conditions along  $x$ :

$$\mathcal{A}(x + L_x, y, z) = \mathcal{A}(x, y, z). \quad (2.6)$$

Given the periodicity along  $x$  and  $y$  expressed by equations (2.6) and (2.4), a Fourier series decomposition is a practical representation of fluctuation fields as it naturally

verifies these boundary conditions. Such a Fourier representation reads:

$$\mathcal{A}(x, y, z) = \sum_{k_x, k_y} \hat{\mathcal{A}}_{k_x, k_y}(z) \exp[i(k_x x + k_y y)], \quad (2.7)$$

with  $k_x$  and  $k_y$  corresponding in general to all harmonics of the minimum wave numbers  $k_{x, \min} = 2\pi/L_x$  and  $k_{y, \min} = 2\pi/L_y$  respectively.

The underlying axisymmetry of a tokamak corresponds to an invariance of the unperturbed system with respect to  $\varphi$  in  $(\psi, \chi, \varphi)$  coordinates. This translates to an invariance with respect to  $y$  in  $(x, y, z)$  coordinates. Consequently, any fluctuating field related to a *linear* eigenmode of the toroidal system is thus composed of a single  $k_y$  Fourier mode. Note that a given  $k_y$  wave number is equivalent to a toroidal wave number  $n$  according to the relation

$$n = -k_y C_y. \quad (2.8)$$

It remains to express the pseudo-periodic boundary condition (2.5) in the Fourier representation (2.7). In doing so, one considers the  $x$ -dependence of the safety factor profile  $q_s(x)$ . This is essential to ensure that the flux-tube model contains the information on the radial position of MRSs related to a  $k_y$  mode and thus accounts for the particular dynamics, in particular resonances, that can take place at such surfaces. This is of key importance to the study carried out in this paper. Accounting for the  $x$ -dependence of the safety factor in these boundary conditions is thus an exception in the flux-tube framework, as all other background and magnetic geometry coefficients, as already mentioned, are assumed  $x$ -independent. Only a *linearised* safety factor profile of the form:

$$q_s(x) = q_0[1 + \hat{s}(x - x_0)/r_0], \quad (2.9)$$

with  $\hat{s}$  standing for the magnetic shear, is in fact compatible with the Fourier representation along  $x$ . For a given  $k_y$  Fourier mode, inserting (2.7) and (2.9) into (2.5) leads to

$$\sum_{k_x} \hat{\mathcal{A}}_{k_x, k_y}(z + 2\pi) \exp[2\pi i k_y C_y q_s(x = 0)] \exp[i(k_x + 2\pi k_y \hat{s})x] = \sum_{k_x} \hat{\mathcal{A}}_{k_x, k_y}(z) \exp(ik_x x). \quad (2.10)$$

For convenience and without further loss of generality, one assumes here that the origin of the  $x$  coordinate corresponds to the lowest order MRS (LMRS), *i.e.* a MRS related to  $k_{y, \min}$ . This condition reads:

$$k_{y, \min} C_y q_s(x = 0) = n_{\min} q_s(x = 0) = n_{\min} q_0(1 - \hat{s}x_0/r_0) \in \mathbb{Z},$$

with  $n_{\min}$  the toroidal wave number associated to  $k_{y, \min}$ . Note that this relation provides an equation for the shift in  $x_0$  and ensures that the phase factor  $\exp[2\pi i k_y C_y q_s(x = 0)] = 1$  for all  $k_y$  modes. Based on (2.10), the boundary condition in  $z$  then finally translates for a given  $k_y$  Fourier mode to the following coupling between  $k_x$  Fourier modes:

$$\hat{\mathcal{A}}_{k_x, k_y}(z + 2\pi) = \hat{\mathcal{A}}_{k_x + 2\pi k_y \hat{s}, k_y}(z). \quad (2.11)$$

The coupling between  $k_x$  Fourier modes can also be understood as follows. In a sheared toroidal system, the wave vector associated to a Fourier mode  $(k_x, k_y)$  is given by

$$\vec{k} = k_x \nabla x + k_y \nabla y = (k_x + k_y \hat{s} z) \nabla x - n q_s \nabla \chi + n \nabla \varphi, \quad (2.12)$$

having used relations (2.2) and (2.8). After one poloidal turn ( $z \rightarrow z + 2\pi$ ), the wave vector (2.12) obviously becomes the one associated to the Fourier mode  $(k_x + 2\pi k_y \hat{s}, k_y)$ , thus explaining the coupling of  $k_x$  modes.



One should emphasize that this coupling resulting from the parallel boundary condition applies to any fluctuating field and in particular already to linear eigenmodes of the system and is thus of different physical nature than the three Fourier mode ( $\sim 3$ -wave) interaction discussed later on, resulting from non-linear dynamics.

A linear eigenmode with fixed  $k_y$  thus couples to a set of  $k_x = k_{x0} + p 2\pi k_y \hat{s}$ ,  $p \in \mathbb{Z}$ , modes and is of the form:

$$\mathcal{A}(x, y, z) = \exp(ik_y y) \sum_{p=-\infty}^{+\infty} \hat{\mathcal{A}}_{k_{x0}+p2\pi k_y \hat{s}, k_y}(z) \exp[i(k_{x0} + p 2\pi k_y \hat{s})x]. \quad (2.13)$$

One can show that this form is equivalent to the so-called ballooning representation (Connor *et al.* 1978; Hazeltine & Newcomb 1990):

$$\mathcal{A}(\psi, \chi, \varphi) = \sum_{p=-\infty}^{+\infty} \hat{\mathcal{A}}_b(\chi + p 2\pi) \exp[in(\varphi - q_s(\psi)(\chi + p 2\pi - \chi_0))], \quad (2.14)$$

noting in this relation the ballooning envelope  $\hat{\mathcal{A}}_b(\chi)$ , defined over the extended ballooning space  $\chi \in ]-\infty, +\infty[$ , as well as the field-aligned phase factor including the ballooning angle  $\chi_0$ . The relation between the two representations (2.13) and (2.14) is given by

$$\hat{\mathcal{A}}_b(\chi + p 2\pi) = \hat{\mathcal{A}}_{k_{x0}+p2\pi k_y \hat{s}, k_y}(\chi) \quad (2.15)$$

$$\chi_0 = -k_{x0}/(k_y \hat{s}), \quad (2.16)$$

In a flux-tube of radial extension  $L_x$ , all coupled Fourier modes  $k_x + p 2\pi k_y \hat{s}$  relative to this direction must be harmonics of  $k_{x,\min}$ . This must hold for all  $k_y$  and in particular for the lowest harmonic  $k_{y,\min}$ :

$$2\pi k_{y,\min} \hat{s} = M k_{x,\min} = M \frac{2\pi}{L_x},$$

with  $M \in \mathbb{N}^*$  a strictly positive integer. This relation can be rewritten:

$$L_x = \frac{M}{k_{y,\min} \hat{s}} = M \Delta x_{\text{LMRS}} = \frac{M}{2\pi \hat{s}} L_y, \quad (2.17)$$

thus imposing a constraint between the extensions  $L_x$  and  $L_y$  of the flux tube along the directions  $x$  and  $y$  respectively. In practice, the integer  $M$  must be chosen such that  $L_x$  is larger than the radial correlation length of turbulent eddies.

Relation (2.17) also implies that  $L_x$  must be an integer multiple of  $\Delta x_{\text{LMRS}} = 1/(k_{y,\min} \hat{s})$ , identified as the distance between lowest order MRSs. Indeed, considering the linearised safety factor profile (2.9), the distance  $\Delta x_{\text{MRS}}$  between MRSs corresponding to a given  $k_y \neq 0$  mode is constant and given by

$$1 = \Delta[nq_s(x)] = k_y \hat{s} \Delta x_{\text{MRS}} \implies \Delta x_{\text{MRS}}(k_y) = 1/(k_y \hat{s}),$$

having invoked (2.8). One thus in particular has  $\Delta x_{\text{LMRS}} = \Delta x_{\text{MRS}}(k_{y,\min}) = 1/(k_{y,\min} \hat{s})$ . For a given  $k_y \neq 0$  mode, the radial positions of corresponding MRSs are thus

$$x_{\text{MRS}} = m \Delta x_{\text{MRS}} = m \frac{k_{y,\min}}{k_y} \Delta x_{\text{LMRS}}, \quad m \in \mathbb{Z}.$$

Note that the positions of lowest order MRSs,  $x_{\text{LMRS}} = m \Delta x_{\text{LMRS}}$ , are MRSs to *all*  $k_y \neq 0$  modes. More generally, there tends to be an alignment of the radial positions of MRSs corresponding to the different  $k_y$  around the lowest order MRSs (second order

MRSs are common to every second  $k_y$ , third order MRSs to every third  $k_y$ , etc.) and a misalignment around the higher order MRSs, as shown in figure 4(a). This level of (mis)alignment of MRSs can be measured by their radial density, as shown in figure 12 in (Dominski *et al.* 2017).

Other numerical parameters are as follows. In the  $k_x$  and  $k_y$  Fourier spaces relative to the  $x$  and  $y$  directions, one considers  $N_{k_x}$  and  $N_{k_y}$  Fourier modes respectively. In real space, the simulation volume  $L_x \times L_y \times L_z$  is discretised by  $N_x \times N_y \times N_z$  equidistant grid points such that  $N_x = N_{k_x}$  and  $N_y = 2N_{k_y} - 1$ . Note that by invoking the reality condition, only modes  $k_y \geq 0$  are evolved in GENE. The parallel direction is treated in real space with  $z \in [-L_z/2, +L_z/2[$ . For our study, which in particular addresses a system size effect, it is essential to choose  $L_z = 2\pi$ , *i.e.* considering only one poloidal turn, for consistency with global geometries (Scott 1998). The gyrocenter velocity space coordinates are  $(v_{\parallel}, \mu)$ , where  $\mu = mv_{\perp}^2/2B_0$  is the magnetic moment, and  $v_{\parallel}$  and  $v_{\perp}$  are respectively the velocity components parallel and perpendicular to the magnetic field. For the parallel velocity direction one considers  $v_{\parallel} \in [-v_{\parallel, \max}, +v_{\parallel, \max}]$  with a discretisation involving  $N_{v_{\parallel}}$  equidistant grid points, while for the  $\mu$  direction one considers  $\mu \in [0, \mu_{\max}]$  with a discretisation involving  $N_{\mu}$  grid points following the Gauss-Laguerre integration scheme.

### 3. Non-adiabatic passing electron dynamics leading to stationary zonal structures

This section presents a summary of relevant results from the articles (Dominski *et al.* 2015, 2017), which addressed certain effects of non-adiabatic passing electron dynamics on turbulent transport.

Non-adiabatic passing electron response leads to generation of fine-structures at MRSs which can be first studied in linear simulations. Figure 1 shows the envelope in the  $(x, z)$  plane of the electrostatic potential  $\Phi$  of the unstable linear ITG eigenmode with  $k_y \rho_i = 0.28$ , considering either adiabatic or kinetic electron response, and for the set of physical parameters given in Table 1. This is the same ITG case as considered in reference (Dominski *et al.* 2015) and same numerical grid resolutions have been considered here. While in both cases the modes are ballooned at  $z = 0$ , one observes a fine radial structure at the corresponding MRS (positioned at the center  $x = 0$  of the radial domain) only in the latter case. This is the result of the non-adiabatic passing electron response taking place at MRSs where the parallel wavenumber  $k_{\parallel} \rightarrow 0$  (Chowdhury *et al.* 2008; Dominski *et al.* 2015). In the vicinity of MRSs, the condition for adiabatic electron response is violated as the phase velocity of the eigenmode parallel to the magnetic field becomes greater than the electron thermal velocity:  $|\omega/k_{\parallel}| > v_{\text{th},e}$ . These fine structures along the  $x$  direction translate to a broad range of significant  $k_x$  Fourier modes, *i.e.* to a broad ballooning structure according to equation (2.15), which is referred to as the “giant electron tails” in (Hallatschek & Dorland 2005); see figure 2. No such broad tails in the ballooning structure are observed with adiabatic electrons. Figure 3 plots the  $k_y$  spectrum of linear growth rates  $\gamma$  and real frequencies  $\omega_R$  of most unstable eigenmodes for the cases considered here. Note that  $\omega_R > 0$  corresponds in GENE convention to a mode propagating in the ion-diamagnetic direction, as expected for ITG instabilities.

The radial structures related to the non-adiabatic passing electron dynamics have been shown to persist in the non-linear turbulent regime, as discussed in references (Waltz *et al.* 2006; Dominski *et al.* 2015, 2017). Studies by Dominski *et al.* (2015, 2017), based on both local (flux-tube) and global gyrokinetic simulations, have furthermore shown that, for each fluctuation mode with mode number  $k_y$ , the corresponding MRSs act as

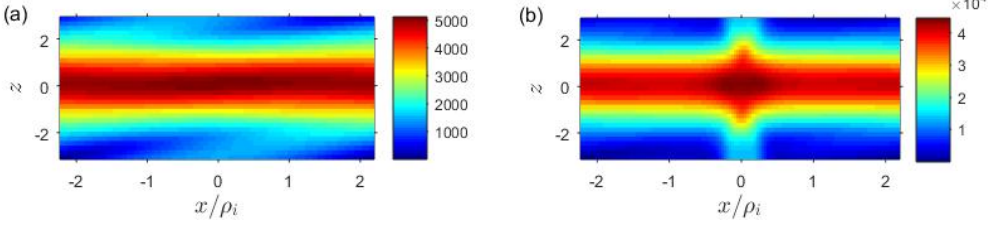


FIGURE 1. Linear eigenmode with  $k_{x0} = 0$  and  $k_y \rho_i = 0.28$ , in the case of (a) adiabatic, (b) kinetic electron response. Shown is the  $(x, z)$ -dependence of the electrostatic potential  $\Phi$  in absolute value, weighted by the Jacobian,  $J|\Phi|$ .

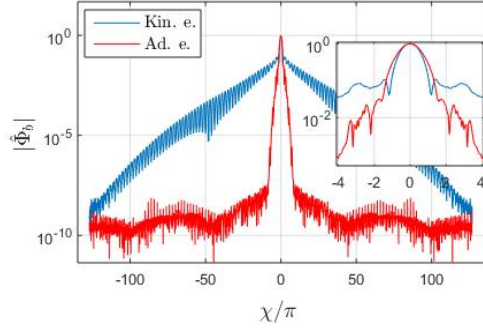


FIGURE 2. Ballooning representation  $|\hat{\Phi}_b(\chi)|$  of the electrostatic potential  $\Phi$  for the same linear eigenmode as in figure 1, showing both the case of kinetic (blue) and adiabatic (red) electrons. Inset figure shows the zoom near  $\chi = 0$ .

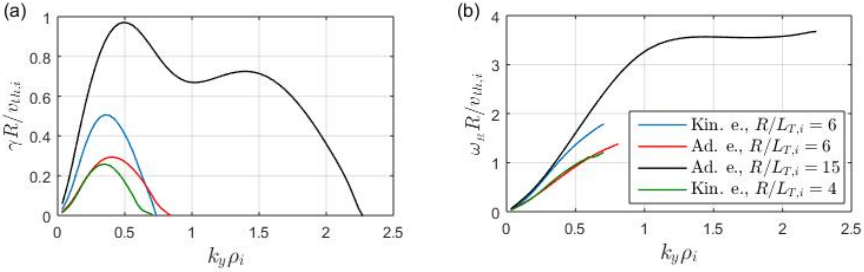


FIGURE 3. (a) Linear growth rate  $\gamma$  and (b) real frequency  $\omega_R$  in units of  $v_{th,i}/R$  as a function of  $k_y \rho_i$ . Adiabatic electron simulations with  $R/L_{T,i} = 6$  and  $15$  are plotted in red and black respectively. Kinetic electron simulations with  $R/L_{T,i} = 4$  and  $6$  are plotted in green and blue respectively.

radially localized transport channels. This is illustrated in figures 4(a,b). Radial regions with high (resp. low) density of MRSs thus tend to lead to high (resp. low) particle and heat diffusivities. Consequently, to ensure radially constant time-averaged total particle and heat fluxes, density and temperature gradients (driving the turbulence) become corrugated, steepening in regions with low density of MRSs and flattening in regions with high density of MRSs. See figures 4(c,d) where the time-averaged density gradient and particle flux are shown as a function  $x$ .

Stationary  $E \times B$  shear flow layers associated to the time-averaged radial electric field are also observed (see figure 5 where the corresponding effective shearing rate as defined

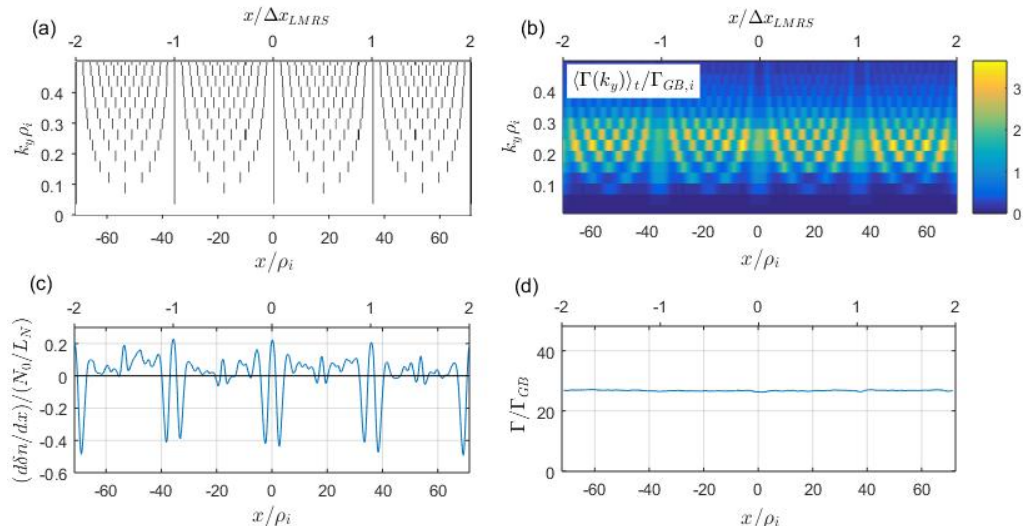


FIGURE 4. (a) Radial position of MRSs for each  $k_y$  mode, (b) radial dependence of contribution to time-averaged particle flux  $\Gamma$  in gyro-Bohm units  $\Gamma_{GB} = N_0 v_{th,i} (\rho_i/R)^2$  from each  $k_y$  mode, (c) radial gradient of flux-surface and time-averaged density fluctuation  $\delta n$  normalised with respect to  $N_0/L_N$  (positive/negative values correspond resp. to flattening/steepening of profiles), and (d) radial profile of time-averaged total particle flux (summed over all  $k_y$ ). All subplots correspond to kinetic electron simulation for the parameter set given in table 1, with  $k_{y,\min}\rho_i = 0.035$  and  $R/L_{T,i} = 6$ . Ticks  $x/\Delta x_{LMRS} = \{-2, -1, 0, 1, 2\}$  on the top axes denote the lowest order MRSs (LMRSs).

in (4.1) is plotted). This electric field component ensures the radial force balance with the pressure gradients related to the corrugation of density and temperature profiles (Waltz *et al.* 2006). In sections 5.3 - 5.5, it is shown that these stationary shear structures are actually driven by a contribution to the Reynolds Stress coming from the so-called self-interaction mechanism (Weigl *et al.* 2018).

#### 4. $k_{y,\min}\rho_i$ scan in ITG-driven turbulence. Role of stationary and fluctuating components of zonal shear flows

Non-linear simulations have been carried out considering conditions of ITG-driven turbulence. Reference physical and numerical parameters for these simulations are summarized in table 1. The physical parameters are close to the Cyclone Base Case (CBC) (Dimitis *et al.* 2000), with background gradients slightly modified to eliminate unstable TEM and ETG modes. Compared to typical flux-tube runs, a high radial resolution is chosen (with radial grid-points  $N_x = 512$ ) in order to ensure that the dynamics at MRSs (separated by a radial distance  $\Delta x_{MRS} = 1/\hat{s}k_y$  for a given  $k_y$ ) is very well resolved, as discussed in detail in Ref. (Dominski *et al.* 2015). In our work, this high  $x$ -resolution is all the more critical since the fine-structures forming at the MRSs play an important role in the self-interaction mechanism, which is crucial to our study.

A scan in  $k_{y,\min}\rho_i$  is performed while keeping both  $k_{y,\max}\rho_i$  and  $L_x/\rho_i$  fixed. Successively halving  $k_{y,\min}\rho_i$ , the values  $k_{y,\min}\rho_i = 0.14, 0.07, 0.035$ , and  $0.0175$  have been considered. Note that these values for  $k_{y,\min}\rho_i$  span the typical range  $10^{-2} - 10^{-1}$  considered in practice when carrying out ion-scale flux-tube simulations. To keep  $k_{y,\max}\rho_i$  fixed, the total number  $N_y$  of  $k_y$  modes must thus be doubled between consecutive runs, whereas to keep  $L_x/\rho_i$  fixed, the number  $M$  of lowest order MRSs contained in the

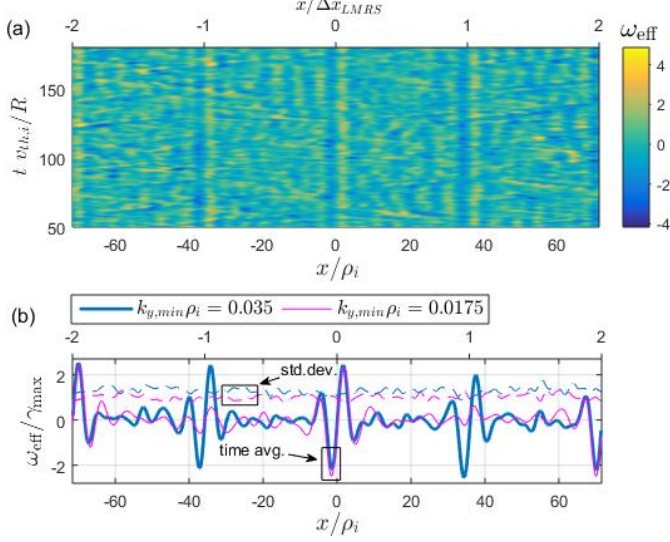


FIGURE 5. (a) Effective shearing rate  $\omega_{\text{eff}}(x, t)$  plotted as a function of the radial position  $x$  and time  $t$ , for the kinetic electron simulation with parameters as given in table 1,  $k_{y,\text{min}}\rho_i = 0.035$  and  $R/L_{T,i} = 6$ . (b) Solid blue line indicates the associated time-averaged component  $\langle \omega_{\text{eff}} \rangle_t$ , normalised by the corresponding maximum linear growth rate  $\gamma_{\text{max}}$ , at each radial position  $x$ . Dashed blue line indicates the standard deviation  $\text{SD}_t(\omega_{\text{eff}})(x) = [\langle (\omega_{\text{eff}} - \langle \omega_{\text{eff}} \rangle_t)^2 \rangle_t]^{1/2}$  in time, normalised by  $\gamma_{\text{max}}$ . For comparison, results for  $k_{y,\text{min}}\rho_i = 0.0175$  have been added in magenta.

---

Geometry: Ad-hoc concentric circular geometry(Lapillonne *et al.* 2009)

$\epsilon = 0.18$	$q_0 = 1.4$	$\hat{s} = 0.8$	$\beta = 0.001$	
$m_i/m_e = 400$	$T_e/T_i = 1.0$	$R/L_N = 2.0$	$R/L_{T_i} = 6.0$	$R/L_{T_e} = 2.0$
$L_x = 142.9 \rho_i$	$L_y^* = 179.5 \rho_i$	$L_z = 2\pi$	$v_{\parallel,\text{max}} = 3\sqrt{2} v_{\text{th},i}$	$\mu_{\text{max}} = 9 T_i/B_{0,\text{axis}}$
$M^* = 4$	$N_{k_x} \times N_{k_y}^* \times N_z \times N_{v_{\parallel}} \times N_{\mu} = 512 \times 128 \times 16 \times 64 \times 9$			

TABLE 1. Parameter set for non-linear simulations. The parameter  $k_{y,\text{min}} = 2\pi/L_y$  is scanned and takes the values  $k_{y,\text{min}}\rho_i \in \{0.14, 0.07, 0.035, 0.0175\}$ , while  $k_{y,\text{max}} = k_{y,\text{min}}N_y/2$  and  $L_x = M/\hat{s}k_{y,\text{min}}$  are kept constant. The values indicated in the table correspond to the particular case  $k_{y,\text{min}}\rho_i = 0.035$ . Asterisks indicate variables which vary during the  $k_{y,\text{min}}\rho_i$  scan.  $v_{\text{th},i} = \sqrt{T_i/m_i}$  stands for the ion thermal velocity and  $B_{0,\text{axis}}$  for the magnetic field on axis.

---

simulation box is halved. The parameter  $M$  thus takes on the respective values  $M = 16, 8, 4$  and  $2$ . The case  $k_{y,\text{min}}\rho_i = 0.07$  is in fact equivalent to the ITG case already studied by Dominski *et al.* (2015).

Based on the relation  $k_{y,\text{min}}\rho_i = (q_0 a/r_0)\rho^*$  (assuming that all toroidal modes are accounted for, so that  $n_{\text{min}} = 1$ ) and for the typical mid-radius value  $r_0/a = 0.5$  and here considered  $q_0 = 1.4$ , one obtains  $\rho^* = 5.0 \cdot 10^{-2}, 2.5 \cdot 10^{-2}, 1.25 \cdot 10^{-2}, 6.25 \cdot 10^{-3}$ . Note for reference that typical values for this parameter are  $\rho^* \simeq 1 \cdot 10^{-2}$  in a smaller-size machine such as the TCV tokamak,  $\rho^* \simeq 3 \cdot 10^{-3}$  in the DIII-D tokamak(Waltz 2005), while the projected values for ITER are still an order of magnitude smaller.

In order to address how the results from the  $k_{y,\text{min}}\rho_i$  scan depend on whether one is near

or far from marginal stability, the scan was repeated for a second ion temperature gradient in both the adiabatic and kinetic electron cases. To this end, carrying out preliminary  $R/L_{T_i}$  scans for  $k_{y,\min}\rho_i = 0.035$ , the non-linear (Dimits-shifted) critical temperature gradients  $R/L_{T_i,\text{crit}}$  were first identified. For adiabatic electrons,  $R/L_{T_i,\text{crit}} = 5.5$  was found, so that the reference case temperature gradient  $R/L_{T_i} = 6$  is relatively *near* marginal stability and the second  $k_{y,\min}\rho_i$  scan was therefore performed for  $R/L_{T_i} = 15$  in this case, *i.e.* *farther* from marginal stability. For kinetic electrons,  $R/L_{T_i,\text{crit}} = 3.5$ , so that the reference case temperature gradient  $R/L_{T_i} = 6$  is relatively *far* from marginal stability and the second  $k_{y,\min}\rho_i$  scan was therefore performed for  $R/L_{T_i} = 4$  in this case, *i.e.* *nearer* marginal stability.

To ensure that the simulations results are sound, convergence tests with respect to radial box size  $L_x$  and the numerical resolutions  $N_z$ ,  $N_{v_{\parallel}}$  and  $N_{\mu}$  were carried out. Convergence test on  $N_x$  had already been addressed in Dominski *et al.* (2015). Based on these tests, the turbulent heat and particle fluxes, as well as statistical properties of  $E \times B$  shearing rates are estimated to be within  $\sim 10\%$  of their converged value. Benchmarking of the GENE results with the gyrokinetic code GS2 (Dorland *et al.* 2000) was furthermore performed for a limited number of simulations. Although a reduced mass ratio is considered here, similar results have been obtained with the physical mass ratio of hydrogen  $m_i/m_e = 1836$ .

First results from the  $k_{y,\min}\rho_i$  scan will now be discussed. Given their importance in saturating ITG turbulence, particular attention will be given to the statistical properties of the shearing rate  $\omega_{E \times B}$  associated to the to zonal  $E \times B$  flows. We will in fact consider the effective shearing rate  $\omega_{\text{eff}}$ , similar to that defined in (Dominski *et al.* 2015). This rate is estimated as follows. One first defines the zonal  $E \times B$  shearing rate experienced by the ions, which are the dominant instability drivers in the case of the here considered ITG turbulence:

$$\omega_{E \times B, \text{ion}}(x, t) = \frac{1}{B_0} \frac{\partial^2 \langle \bar{\Phi} \rangle_{y,z}}{\partial x^2},$$

where the flux-surface average  $\langle \bar{\Phi} \rangle_{y,z}$  provides the zonal component of  $\bar{\Phi}$  and involves both an average over  $y$ ,  $\langle \cdot \rangle_y = (1/L_y) \int_0^{L_y} \cdot dy$ , and an average over  $z$ ,  $\langle \cdot \rangle_z = \int_{-\pi}^{+\pi} \cdot J^{xyz} dz / \int_{-\pi}^{+\pi} J^{xyz} dz$ .  $\bar{\Phi}$  is the scalar potential gyroaveraged over the Maxwellian ion background velocity distribution. The shearing rate  $\omega_{E \times B, \text{ion}}$  is then furthermore averaged over a small time window of width  $\tau$ , given that fluctuations that are very short-lived in time do not contribute effectively towards the zonal flow saturation mechanism (Hahm *et al.* 1999), thus providing the effective shearing rate:

$$\omega_{\text{eff}}(x, t) = \frac{1}{\tau} \int_{t-\tau/2}^{t+\tau/2} \omega_{E \times B, \text{ion}}(x, t') dt'. \quad (4.1)$$

Here,  $\tau = 1/\gamma_{\text{max}}$  is considered, where  $\gamma_{\text{max}}$  is the growth rate of the most unstable linear mode.

As an illustration, the effective shearing  $\omega_{\text{eff}}(x, t)$  has been plotted in figure 5(a) as a function of  $x$  over the full flux-tube width  $L_x$  and as a function of  $t$  over the simulation time slice  $50 < t v_{\text{th},i}/R < 180$ . Shown is the case with kinetic electrons,  $R/L_{T_i} = 6$  and  $k_{y,\min}\rho_i = 0.035$ . The radial profile for the time-averaged component  $\langle \omega_{\text{eff}} \rangle_t(x)$ , is shown in figure 5(b). For comparison, the same profile is also shown for the same physical parameters except for  $k_{y,\min}\rho_i = 0.0175$ .

The system average of the *total* effective shearing rate is plotted in figure 6(a) as a function of  $k_{y,\min}\rho_i$ , considering a log-log scale. This average value is provided by the

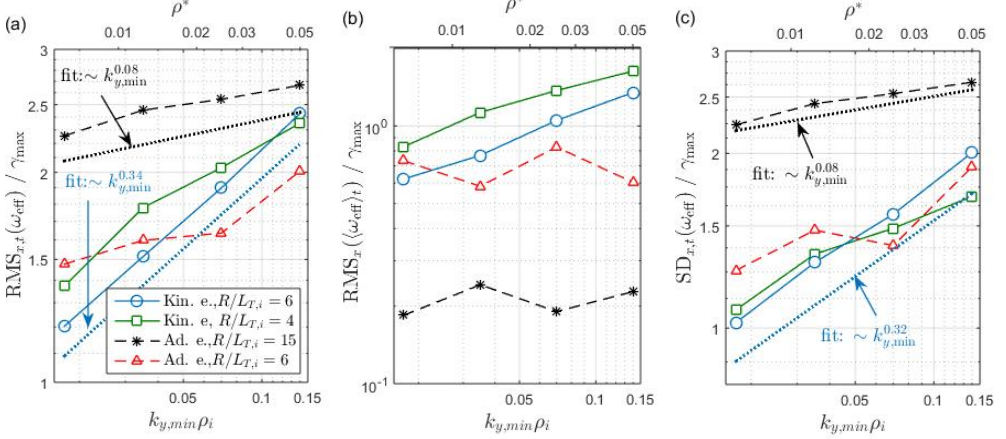


FIGURE 6. Effective shearing rate  $\omega_{\text{eff}}$  associated to the zonal  $E \times B$  flows, normalised to corresponding maximum linear growth rate  $\gamma_{\text{max}}$ , as a function of  $k_{y,\text{min}}\rho_i$ . Solid lines denote kinetic electron simulations for  $R/L_{T,i} = 4$  (green squares) and 6 (blue circles) respectively. Dashed lines denote adiabatic electron simulations for  $R/L_{T,i} = 6$  (red triangles) and 15 (black stars) respectively. Other parameters remain the same as in table 1. (a) System average of total shearing rate  $\text{RMS}_{x,t}(\omega_{\text{eff}}) = (\langle \omega_{\text{eff}}^2 \rangle_{x,t})^{1/2}$ . (b) Contribution from the stationary component,  $\text{RMS}_x(\langle \omega_{\text{eff}} \rangle_t) = [\langle (\langle \omega_{\text{eff}} \rangle_t)^2 \rangle_x]^{1/2}$ . (c) Contribution from fluctuation component,  $\text{SD}_{x,t}(\omega_{\text{eff}}) = [\langle (\omega_{\text{eff}} - \langle \omega_{\text{eff}} \rangle_t)^2 \rangle_{x,t}]^{1/2}$ . All plots in log-log scale.

Root Mean Square (RMS) estimate:

$$\text{RMS}_{x,t}(\omega_{\text{eff}}) = (\langle \omega_{\text{eff}}^2 \rangle_{x,t})^{1/2}, \quad (4.2)$$

involving both a radial average,  $\langle \cdot \rangle_x = (1/L_x) \int_0^{L_x} \cdot dx$ , and an average over the whole simulation time  $t_{\text{sim}}$ ,  $\langle \cdot \rangle_t = (1/t_{\text{sim}}) \int_0^{t_{\text{sim}}} \cdot dt$ . Figure 6(a) shows results for the scans carried out for the two respective temperature gradients  $R/L_{T,i}$  considered for both adiabatic and kinetic electrons. The shearing rates have been normalised with respect to the value of  $\gamma_{\text{max}}$ , which takes on different values for the four considered datasets (see figure 3). Normalised shearing values  $\omega_{\text{eff}}/\gamma_{\text{max}} \gtrsim 1$  can be considered as significant for saturating ITG-driven turbulence. Note that a straight system average  $\langle \omega_{\text{eff}}(x,t) \rangle_{x,t}$  of the shearing rate would converge to zero over sufficiently long simulation time, which is why the RMS estimate (4.2) is considered. One notes that, over the considered range  $10^{-2} - 10^{-1}$  in  $k_{y,\text{min}}\rho_i$  values, the total effective shearing rate  $\text{RMS}_{x,t}(\omega_{\text{eff}})$  decreases in all cases with decreasing  $k_{y,\text{min}}\rho_i$ , *i.e.* with increasing machine size. However, significantly stronger scaling is observed for the scans with kinetic compared to adiabatic electrons. As can be seen from the log-log plot, the shearing rate appears to roughly scale as  $\sim (k_{y,\text{min}}\rho_i)^\alpha$ ,  $\alpha > 0$ . This scaling is particularly evident for the kinetic electron case far from marginal stability ( $R/L_{T,i} = 6$ ), for which  $\alpha \simeq 0.34$ . Similar scaling is observed nearer marginal stability ( $R/L_{T,i} = 4$ ) as well. The adiabatic electron scans however show a weaker scaling with  $\alpha \simeq 0.08$  for both  $R/L_{T,i} = 6$  and  $R/L_{T,i} = 15$ .

Figure 7(a) plots in log-log scale, the time and flux-tube -averaged radial ion heat flux  $Q_i$  as a function of  $k_{y,\text{min}}\rho_i$ . Heat fluxes have been normalised to gyro-Bohm units  $Q_{GB,i} = n_{0,i}T_i v_{\text{th},i}(\rho_i/R)^2$ . Results for all four considered datasets are again presented. Over the considered range of  $k_{y,\text{min}}\rho_i$ , fluxes appear not to be converged with respect to this parameter. This non-convergence is particularly striking for both



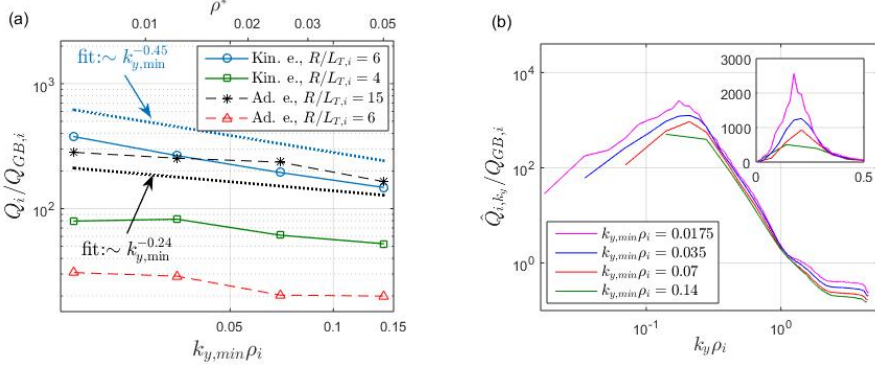


FIGURE 7. (a) Log-log plot of the time-averaged and gyro-Bohm normalised ion heat flux  $Q_i$  as a function of  $k_{y,\min}\rho_i$ . Same cases as considered in figure 6. (b) Log-log plot of  $k_y$  spectra of ion heat flux  $Q_i$  for the kinetic electron runs with  $R/L_{T,i} = 6$  and  $k_{y,\min}\rho_i = 0.0175$  (magenta), 0.035 (blue), 0.07 (red) and 0.14 (green). Inset figure shows lin-lin plot of the zoom near the peaks.

adiabatic and kinetic electron simulations for the respective ion temperature gradients far from marginal stability. As can be seen from the log-log plot, in these cases one observes a scaling  $Q_i/Q_{GB,i} \sim (k_{y,\min}\rho_i)^{-\alpha}$ ,  $\alpha > 0$ , with  $\alpha = 0.45$  (kin.e.,  $R/L_{T,i} = 6$ ) and 0.24 (ad.e.,  $R/L_{T,i} = 15$ ).

To provide insight into which wavelengths mainly contribute to the increasing heat flux as  $k_{y,\min}\rho_i$  decreases, the heat flux  $k_y$ -spectra is plotted in figure 7(b) for the set of simulations corresponding to the  $k_{y,\min}\rho_i$  scan with kinetic electrons and  $R/L_{T,i} = 6$ .  $Q_{i,k_y}$  is defined such that total heat flux  $Q_i = \sum_{k_y} Q_{i,k_y} dk_y$ , where  $dk_y = k_{y,\min}$ . One observes that all spectra present a peak at  $k_y\rho_i \simeq 0.2$  and that the increase in heat flux as  $k_{y,\min}\rho_i \rightarrow 0$  is not carried by the ever smaller minimum wavenumbers but by the contributions of modes  $0.07 \leq k_y\rho_i \leq 0.35$  in the vicinity of the peak (contributing to at least 90% of the heat flux), range fully covered by all simulations, except for the largest considered  $k_{y,\min}\rho_i = 0.14$ . Note that the inertial range ( $k_y\rho_i \gtrsim 0.35$ ) remains essentially identical over all runs.

*A priori*, a straightforward explanation for the decreasing  $E \times B$  shearing rate leading to increased heat fluxes as  $k_{y,\min}\rho_i$  decreases, is the reduction in the radial density of stationary shear layers at LMRSS. Let us indeed recall that the distance between LMRSS is given by  $\Delta x_{\text{LMRS}} = 1/(k_{y,\min}\hat{s})$ . Note as well the remarkable fact that the radial width and amplitude of the shear layers at LMRSS remains essentially invariant when varying  $k_{y,\min}\rho_i$ , as illustrated in figure 5(b). The contribution to the total shearing rate estimate (4.2) from the stationary component of the shearing rate profile  $\langle \omega_{\text{eff}} \rangle_t(x)$  can be calculated by:

$$\text{RMS}_x(\langle \omega_{\text{eff}} \rangle_t) = \left[ \langle (\langle \omega_{\text{eff}} \rangle_t)^2 \rangle_x \right]^{1/2}, \quad (4.3)$$

and has been plotted in log-log scale as a function of  $k_{y,\min}\rho_i$  in figure 6(b). As expected, this system average of the stationary shearing rate profile decreases algebraically for kinetic electron simulations with decreasing  $k_{y,\min}$ , while for the adiabatic electron simulations there is no obvious dependence on  $k_{y,\min}\rho_i$  as the mechanism developing the prominent fine stationary structures on  $\langle \omega_{\text{eff}} \rangle_t(x)$  is absent in this case.

This explanation for the increase of turbulent fluxes as a result of the decrease in the radial density of stationary zonal  $E \times B$  shear layers is however not satisfactory at closer scrutiny. This is made clear by the results presented in figure 8, where the radial



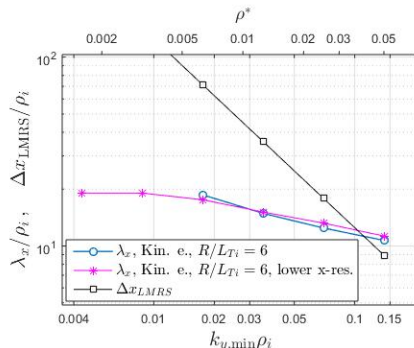


FIGURE 8. Blue circles denote the radial correlation length  $\lambda_x$  of turbulent eddies in units of  $\rho_i$  as a function of  $k_{y,\min}\rho_i$  for kinetic electron simulations and  $R/L_{T_i} = 6$  (all parameters as given in table 1). Magenta asterisks correspond to results obtained with the same parameters except for a decreased radial resolution (by a factor 4), which enabled to carry out runs with  $k_{y,\min}\rho_i$  values as low as  $\sim 5 \cdot 10^{-3}$  (these simulations are discussed in more detail in relation with Fig. 18). Distance  $\Delta x_{LMRS} = 1/(k_{y,\min}\hat{s})$  between LMRSSs is plotted with black squares.

correlation length of turbulent eddies  $\lambda_x$  is plotted as a function of  $k_{y,\min}\rho_i$  for the case with kinetic electrons and  $R/L_{T_i} = 6$ . The radial correlation length is defined as  $\lambda_x = \langle \lambda_x(y) \rangle_y$ , with  $\lambda_x(y)$  estimated as that smallest value of  $\Delta x$  for which the auto-correlation function  $R(\Delta x, y) = \int \Phi'^*(x - \Delta x, y) \Phi'(x, y) dx$  is  $1/e$  times its maximum value (this maximum is reached for  $\Delta x = 0$  and  $e$  is the base of the natural logarithm).  $\Phi'(x, y)$  is the scalar potential evaluated at the outboard midplane, with the zonal ( $k_y = 0$ ) component removed:  $\Phi'(x, y) = \Phi(x, y, z = 0) - \langle \Phi(x, y, z = 0) \rangle_y$ . This radial correlation length increases as  $k_{y,\min}\rho_i$  decreases, but with a much weaker scaling (fit provides  $\lambda_x/\rho_i \sim k_{y,\min}\rho_i^{-0.27}$  over the considered range  $k_{y,\min}\rho_i = 10^{-2} - 10^{-1}$ ) than the increase of the distance  $\Delta x_{LMRS}/\rho_i \sim (k_{y,\min}\rho_i)^{-1}$  between the main stationary shear layers located at LMRSSs. Below a sufficiently small value of  $k_{y,\min}\rho_i$ , one thus clearly has  $\lambda_x \ll \Delta x_{LMRS}$ . That is, the turbulent eddies are getting actively sheared and broken *in between* low order MRSs where the stationary zonal shear flows are insignificant. The stationary shear layers are therefore not expected to play a major role in the saturation of turbulence as  $k_{y,\min}\rho_i \rightarrow 0$ . We therefore conclude that as  $k_{y,\min}\rho_i \rightarrow 0$ , the saturation of turbulence through the break-up of turbulent eddies is mainly to be attributed to the *fluctuating* component of zonal flows. This is discussed in detail in the following.

The time dependent component (as opposed to the stationary component) of the  $E \times B$  zonal flow and associated shearing rate thus appears to control the saturation of turbulence and related flux levels *between* LMRSSs. An estimate for the amplitude of this fluctuating part of the shearing rate is provided by computing the radial profile of the Standard Deviation  $SD_t(\omega_{\text{eff}})$  of  $\omega_{\text{eff}}$  around the stationary component  $\langle \omega_{\text{eff}} \rangle_t$ :

$$SD_t(\omega_{\text{eff}})(x) = \left[ \langle (\omega_{\text{eff}} - \langle \omega_{\text{eff}} \rangle_t)^2 \rangle_t \right]^{1/2}$$

The radial dependence of  $SD_t(\omega_{\text{eff}})$  has been added to figure 5(b) for the cases with kinetic electrons,  $R/L_{T_i} = 6$  and both  $k_{y,\min}\rho_i = 0.035$  and  $k_{y,\min}\rho_i = 0.0175$ . Based on figure 5(b), it appears that the fluctuating part of the shearing rate remains essentially constant across the radial extent of the system. Furthermore, its amplitude for the considered values of  $k_{y,\min}\rho_i$  still remains significant, *i.e.* larger then  $\gamma_{\text{max}}$ , and of the same order as the maximum amplitude of the time-averaged  $\langle \omega_{E \times B} \rangle_t$  structures. A decrease of

the fluctuating component with decreasing  $k_{y,\min}\rho_i$  is also observed. This is summarized in figure 6(c), where the radial average of the fluctuating component, estimated by

$$\text{SD}_{x,t}(\omega_{\text{eff}}) = \left[ \langle (\omega_{\text{eff}} - \langle \omega_{\text{eff}} \rangle_t)^2 \rangle_{x,t} \right]^{1/2}, \quad (4.4)$$

has been plotted. While  $\text{SD}_{x,t}(\omega_{\text{eff}})$  decreases with  $k_{y,\min}\rho_i$  in both adiabatic and kinetic electron simulations, the scaling is much stronger in the latter case. For instance, in the considered range of  $k_{y,\min}\rho_i$ ,  $\text{SD}_{x,t}(\omega_{\text{eff}}) \sim (k_{y,\min}\rho_i)^\alpha$ , where  $\alpha = 0.08$  for the case with adiabatic electrons at  $R/L_{Ti} = 15$  while  $\alpha = 0.32$  for the case with kinetic electrons at  $R/L_{Ti} = 6$ .

Note that according to the definitions (4.2), (4.3) and (4.4), one has

$$[\text{RMS}_{x,t}(\omega_{\text{eff}})]^2 = [\text{RMS}_x(\langle \omega_{\text{eff}} \rangle_t)]^2 + [\text{SD}_{x,t}(\omega_{\text{eff}})]^2.$$

The decrease of both the fluctuation level of the shearing rate, shown in figure 6(c), along with the decrease in the density of stationary shearing layers at LMRs, reflected by figure 6(b), thus provides a more complete picture of the decrease in the total system average of the shearing rate  $\omega_{\text{eff}}$  as  $k_{y,\min}\rho_i$  decreases, shown in figure 6(a). While the reason for the decrease in the contribution to the shearing rate from stationary zonal flows has already been discussed and is relatively obvious, the reason for the decrease of the contribution from fluctuating zonal flows is not. To explain the latter, it is necessary to understand and analyze the different mechanisms driving the zonal flows. This is done in the following section.

## 5. Analyzing zonal flow drive

In this section, the drive of zonal flows via the two main mechanisms, the modulational instability and self-interaction, are studied. In particular, the statistical properties of these different zonal flow drives are analysed using various diagnostics techniques, with the primary objective of understanding why the fluctuating zonal flow levels decrease with decreasing  $k_{y,\min}\rho_i$  as seen in figure 6(c).

In order to ensure a systematic study, this section has been organised as follows. To start, it is essential to identify the physical quantity(ies) representing the drive of zonal flows ( $\sim$  modes  $k_y\rho_i = 0$ ) from turbulence ( $\sim$  modes  $k_y\rho_i \neq 0$ ). In § 5.1, it is found that Reynolds stress can be used as a convenient proxy for quantifying the drive of zonal flows. The two main mechanisms driving zonal flows are then discussed in the following two subsections: a summary of the well known modulational instability mechanism is given in § 5.2, followed by a detailed description of the self-interaction mechanism in § 5.3. These two mechanisms and the nature of their drives are illustrated first in a simple nonlinear set-up, referred to as the “reduced simulations”, in § 5.4. This is followed by providing the evidence for self-interaction and modulational instability in full turbulence simulations, discussed in § 5.5 and § 5.6 respectively. In the latter subsection, using a bicoherence-like analysis and an estimate of the correlation between the different  $k_y$  contributions to Reynolds stress, it is shown that the drive of zonal flows via self-interaction from each  $k_y$  are essentially incoherent and decorrelated, unlike that via modulational instability. This result will then be used in the following § 6, to show how such a decorrelated drive could explain the observed decrease in fluctuating zonal flow levels with decreasing  $k_{y,\min}\rho_i$ .

### 5.1. Reynolds stress as a proxy for the drive of zonal flows

Zonal flows are linearly stable and are driven by turbulence through the quadratic  $\mathbf{E} \times \mathbf{B}$  non-linearity appearing in the gyrokinetic equation. To better understand their

evolution, we will analyze the properties of Reynolds stress (Diamond *et al.* 2005), more exactly the off-diagonal component  $\langle \tilde{V}_x \tilde{V}_y \rangle$  of the Reynolds stress tensor resulting from the combination of fluctuating  $E \times B$  flow components in the radial and poloidal directions. We will justify in the following that this Reynolds stress can be considered as a valid proxy of the zonal flow drive (Weigl *et al.* 2018). By analyzing Reynolds stress we will be able to identify the different possible mechanisms driving zonal flows, their statistical properties, and relative importance.

We start by considering an approximate evolution equation for the shearing rate  $\omega_{E \times B}$  associated to the  $E \times B$  zonal flows. As shown in references (Parra & Catto 2009; Abiteboul *et al.* 2011; Abiteboul 2012), such an equation can be obtained from the radial conservation equation for the total gyrocenter charge density, which in turn is derived by taking the appropriate velocity moment and flux-surface -average of the gyrokinetic equation. The approach in reference (Abiteboul 2012) has been considered here, but starting from the gyrokinetic equation in the limit of the local (flux-tube) delta-f model rather than the global full-f model considered by Abiteboul (2012). Furthermore, assuming the electrostatic limit, invoking  $m_e/m_i \ll 1$ , and making use of the quasi-neutrality equation in the long wavelength approximation (final result thus valid only to second order in  $k_\perp \rho_i$ ), leads to a relation that can be interpreted as a generalized vorticity equation:

$$\frac{\partial}{\partial t}(\Omega + \Pi) = \frac{\partial^2}{\partial x^2}(\mathcal{R} + \mathcal{P}) + \frac{\partial}{\partial x}\mathcal{N}. \quad (5.1)$$

One identifies on the left hand side of equation (5.1) the generalized vorticity term  $\Omega + \Pi$ , composed of the actual vorticity associated to zonal flows and closely related to the zonal flow shearing rate  $\omega_{E \times B}$  (by neglecting the  $z$  dependence of  $B_0$  and  $g^{xx} \simeq 1$ ):

$$\Omega = n_{0,i} m_i \frac{\partial^2}{\partial x^2} \left\langle \frac{g^{xx}}{B_0^2} \Phi \right\rangle_{yz} \simeq \frac{n_{0,i} m_i}{B_0} \omega_{E \times B},$$

as well as a perpendicular pressure term, related to lowest order finite ion Larmor radius effects:

$$\Pi = \frac{m_i}{2q_i} \frac{\partial^2}{\partial x^2} \left\langle \frac{g^{xx}}{B_0^2} P_{\perp,i} \right\rangle_{yz},$$

with the fluctuating part of the perpendicular ion gyrocenter pressure  $P_{\perp,i}$  expressed in terms of the corresponding gyrocenter distribution fluctuation  $\delta f_i$ :

$$P_{\perp,i} = \int \mu B_0 \delta f_i d^3v.$$

On the right hand side of equation (5.1) one identifies the second radial derivative of a term  $\mathcal{R} = (n_{0,i} m_i / C)$  RS, proportional to the Reynolds stress component RS driving zonal flows:

$$\text{RS} = \left\langle \frac{1}{B_0^2} \frac{\partial \Phi}{\partial y} \left( g^{xx} \frac{\partial \Phi}{\partial x} + g^{xy} \frac{\partial \Phi}{\partial y} \right) \right\rangle_{yz}. \quad (5.2)$$

This Reynolds stress term also has a finite Larmor radius correction term  $\mathcal{P}$ , again expressed in terms of  $P_{\perp,i}$ :

$$\mathcal{P} = \frac{m_i}{2q_i C} \left\langle \frac{1}{B_0^2} \left( g^{xx} \frac{\partial \Phi}{\partial x} \frac{\partial P_{\perp,i}}{\partial y} + 2 g^{xy} \frac{\partial \Phi}{\partial y} \frac{\partial P_{\perp,i}}{\partial y} + g^{xx} \frac{\partial \Phi}{\partial y} \frac{\partial P_{\perp,i}}{\partial x} \right) \right\rangle_{yz}.$$

The last contribution on the right hand side of equation (5.1) is the radial derivative of

the so-called neoclassical term  $\mathcal{N}$ , related to both curvature and  $\nabla B$  drifts:

$$\mathcal{N} = - \sum_{\text{species}} \frac{2\pi\mathcal{C}}{m} \left\langle \gamma_2 \frac{\partial B_0}{\partial z} \int dv_{\parallel} d\mu \frac{mv_{\parallel}^2 + \mu B_0}{B_0^2} \left( \delta f + \frac{q\bar{\Phi}}{T_0} f_0 \right) \right\rangle_{yz},$$

with  $f_0$  the Maxwellian background distribution,  $\gamma_2 = g^{xx}g^{yz} - g^{xy}g^{xz}$  and the constant  $\mathcal{C} = B_0/|\nabla x \times \nabla y|$ .

The different terms appearing in (5.1) can be monitored as a diagnostic along a gyrokinetic simulation. For the purpose of verification, this diagnostic was first applied to simple test cases, including the Rosenbluth-Hinton problem (Rosenbluth & Hinton 1998) addressing the linear dynamics of zonal fluctuations [in this case only the linear neoclassical term contributes on the RHS of (5.1)], as well as the non-linear decay of an initially single unstable eigenmode (as discussed in §5.4). For these simple tests, only longer wavelength modes were considered, so as to stay well within the limit  $k_{\perp}\rho_i \ll 1$  assumed for the derivation of relation (5.1).

After this successful initial verification phase, the terms appearing in equation (5.1) were monitored and compared for the fully developed turbulence simulations studied in this paper, considering the reference gradient case  $R/L_{T,i} = 6$ . In order to validate Reynolds stress as a good proxy for the drive of zonal flows, the correlation between  $\Omega \sim \omega_{E \times B}$  and the two non-linear driving terms  $\partial^2 \mathcal{R}/\partial x^2$  and  $\partial^2 \mathcal{P}/\partial x^2$  in (5.1) was estimated over these simulations. To this end, the following correlation estimator between two observables  $a$  and  $b$ , functions of the radial variable  $x$  and time  $t$ , was applied:

$$\text{Corr}(a, b) = \frac{\sigma_{x,t}(a, b)}{\sigma_{x,t}(a) \sigma_{x,t}(b)} = \frac{\langle (a - \langle a \rangle_{x,t}) (b - \langle b \rangle_{x,t}) \rangle_{x,t}}{\sqrt{\langle (a - \langle a \rangle_{x,t})^2 \rangle_{x,t}} \sqrt{\langle (b - \langle b \rangle_{x,t})^2 \rangle_{x,t}}}.$$

Significant correlation estimates were obtained in this way between  $\Omega$  and the Reynolds stress drive term  $\partial^2 \mathcal{R}/\partial x^2$ . Correlation values were found to increase further by considering only the longer wavelength contributions, achieved by filtering out  $|k_x|\rho_i > 0.5$  and  $|k_y|\rho_i > 0.5$  Fourier modes from the signals. This is in agreement with the long wavelength approximation assumed for deriving equation (5.1). The positive correlation values  $\text{Corr} = 0.77$  and  $0.37$  were obtained in this way between  $\Omega$  and  $\partial^2 \mathcal{R}/\partial x^2$  for the adiabatic and kinetic electron turbulence simulations respectively, while the correlation between  $\Omega$  and  $\partial^2 \mathcal{P}/\partial x^2$  provided the values  $\text{Corr} = 0.75$  and  $0.40$  respectively. These results validate considering the Reynolds stress term  $\partial^2 \text{RS}/\partial x^2$  as a proxy for the drive of zonal flow shear  $\omega_{E \times B}$ .

In the following, it will be insightful to consider the contributions from different  $k_y$  Fourier modes components of the fluctuating fields to the Reynolds stress term RS. Relation (5.2) for RS can indeed be written as a sum over  $k_y$ :

$$\text{RS}(x, t) = \sum_{k_y > 0} \hat{\text{RS}}_{k_y}(x, t), \quad (5.3)$$

with the contribution from the  $k_y$  Fourier mode  $\hat{\Phi}_{k_y}(x, z, t) = \frac{1}{L_y} \int_0^{L_y} \Phi \exp(-ik_y y) dy$  given by

$$\hat{\text{RS}}_{k_y}(x, t) = 2 \text{Re} \left[ \left\langle \frac{1}{B_0^2} k_y \hat{\Phi}_{k_y} \left( g^{xx} \frac{\partial \hat{\Phi}_{k_y}^*}{\partial x} + g^{xy} k_y \hat{\Phi}_{k_y}^* \right) \right\rangle_z \right], \quad (5.4)$$

having invoked the reality condition  $\hat{\Phi}_{-k_y} = \hat{\Phi}_{k_y}^*$ . Considering as well the  $k_x$  Fourier

mode decomposition of  $\Phi$ , each of these  $k_y$  contributions can also be written as follows:

$$\hat{R}S_{k_y}(x, t) = 2 \operatorname{Re}\left\{ \sum_{k_x, k''_x} \left\langle \frac{1}{B_0^2} k_y (g^{xx} k''_x + g^{xy} k_y) \hat{\Phi}_{k_x, k_y} \hat{\Phi}_{k''_x, k_y}^* \right\rangle_z \exp[i(k_x - k''_x)x] \right\}, \quad (5.5)$$

illustrating the drive of zonal modes  $(k'_x = k_x - k''_x, 0)$  through non-linear interaction between Fourier modes  $(k_x, k_y)$  and  $(k''_x, k_y)$ , extensively discussed in sections §5.2 and §5.3.

For the study carried out in this paper, it is essential to understand how different drift modes may non-linearly interact to drive zonal flows via Reynolds stress. To start, we recall in the next subsection the basic mechanism underlying the drive of zonal flows in a simple shearless slab system before considering the more complex case of direct interest to us, *i.e.* of a sheared toroidal system.

### 5.2. Modulational instability in shearless slab system

The drive of zonal flows by microturbulence has been extensively studied in the literature considering a simple slab-like plasma confined by a uniform, shearless magnetic field. Such a system was in particular addressed in the original work by Hasegawa & Mima (1978), where a cold fluid model was assumed for ions and an adiabatic response for electrons. In this model, choosing an orthogonal Cartesian coordinate system  $(x, y, z)$ , the magnetic field is aligned along  $z$ ,  $\mathbf{B} = B\mathbf{e}_z$  and the background density inhomogeneities along  $x$ ,  $\nabla n_0 = (dn_0/dx)\mathbf{e}_x$ . The corresponding well-known model equation for the non-linear evolution of the electrostatic potential  $\Phi$  associated to the fluctuating fields describes the essentially two-dimensional drift wave turbulence in the  $(x, y)$  plane perpendicular to the magnetic field. This model equation led to a first understanding of the generation of zonal flows along  $y$ , *i.e.* in the direction both perpendicular to  $\mathbf{B}$  and the direction of inhomogeneity. The emergence of such large scale flows can in particular be explained as the result of an anisotropic inverse cascade of energy related to the conservation of energy and enstrophy in the 2-dimensional turbulence. The emergence of zonal flows can also be understood at the level of elementary non-linear processes as recalled in the following.

In a shearless slab system, the spatial dependence of linear eigenmodes are given by a *single* Fourier mode  $\Phi(x, y) \sim \Phi_{\mathbf{k}} \exp(i\mathbf{k} \cdot \mathbf{x})$ , with  $\mathbf{x} = x\mathbf{e}_x + y\mathbf{e}_y$  and  $\mathbf{k} = k_x\mathbf{e}_x + k_y\mathbf{e}_y$ . The corresponding time dependence is of the form  $\sim \exp(-i\omega_{\mathbf{k}}t)$ , with  $\omega_{\mathbf{k}}$  the eigenfrequency of the mode. In the simple Hasegawa-Mima model, one has  $\omega_{\mathbf{k}} = k_y v_d / (1 + k^2)$ , with  $\mathbf{v}_d = -(T_e/eB)(d \log n_0/dx)\mathbf{e}_y$  these eigenmodes results from the *quadratic* non-linearity in the Hasegawa-Mima equation, related to the  $\mathbf{v}_{E \times B} = (-\nabla\Phi \times \mathbf{B})/B^2$  drift. The elementary non-linear interaction thus involves a *triplet* of Fourier modes  $\mathbf{k}, \mathbf{k}', \mathbf{k}''$  verifying the wave vector matching condition  $\mathbf{k} = \mathbf{k}' + \mathbf{k}''$ , where each of the modes, *e.g.*  $\mathbf{k}$ , is coupled to the two others,  $\mathbf{k}'$  and  $\mathbf{k}''$  in this case. In case of frequency matching  $\omega_{\mathbf{k}} \simeq \omega_{\mathbf{k}'} + \omega_{\mathbf{k}''}$  and under the condition  $k' < k < k''$ , one can have a resonant decay of mode  $\mathbf{k}$ , *i.e.* a transfer of energy from this mode, into the daughter modes  $\mathbf{k}'$  and  $\mathbf{k}''$ . This basic process is referred to as the resonant 3-wave interaction mechanism. One can furthermore show that in the case where mode  $\mathbf{k}$  represents a drift wave, *i.e.* typically with  $|k_y| \gg |k_x|$ , the decay happens preferentially (meaning with a higher growth rate of decay) if one of the daughter wave vectors, *e.g.*  $\mathbf{k}'$ , is (nearly-) aligned along the  $x$  direction,  $|k'_x| \gg |k'_y|$  (Hasegawa *et al.* 1979). The  $E \times B$  flow associated to the daughter mode  $\mathbf{k}'$  is then obviously along  $y$ , thus explaining the emergence of zonal flows in this direction. Such a mode with vector aligned along the direction of inhomogeneity  $\mathbf{e}_x$  is thus referred to as a zonal mode.

Let us still further consider the decay of a pump drift wave  $\mathbf{k} = (k_x, k_y)$ ,  $k_y \neq 0$ , into a zonal mode  $\mathbf{k}' = (k'_x, 0)$  and the second daughter wave  $\mathbf{k}'' = \mathbf{k} - \mathbf{k}' = (k_x - k'_x, k_y)$ , itself a drift wave. The non-linear interaction between the two drift waves  $\mathbf{k}$  and  $\mathbf{k}''$  thus provides the drive to the zonal mode  $\mathbf{k}'$  via the Reynolds stress RS discussed in §5.1, while the non-linear coupling between the original drift wave  $\mathbf{k}$  and zonal mode  $\mathbf{k}'$ , leading to the growth of the daughter drift wave  $\mathbf{k}''$ , actually represents the *shearing* of the drift mode  $\mathbf{k}$  by the zonal flows associated to  $\mathbf{k}'$ .

Variations to the simple Hasegawa-Mima model have been considered in the literature. In particular, the Enhanced Hasegawa-Mima model (Krommes & Kim 2000; Gallagher *et al.* 2012) accounts for the fact that the adiabatic electron response is inhibited for magnetic surface-averaged fluctuations, *i.e.* modes  $\mathbf{k}$  with  $k_y = 0$ , in other words zonal modes, which leads them to having a reduced effective inertia compared to standard drift waves with  $k_y \neq 0$ . This effect results in an amplification of the decay rates of drift waves into zonal modes and thus to an enhancement of corresponding energy transfer.

A further refinement to the basic driving mechanism of zonal flows is obtained by accounting for the fact that given an initial large amplitude drift mode  $\mathbf{k}$ , decaying into a zonal mode  $\mathbf{k}'$ , both triplet interactions  $[\mathbf{k}, \mathbf{k}', \mathbf{k}'' = \mathbf{k} - \mathbf{k}']$  and  $[\mathbf{k}, -\mathbf{k}', \mathbf{k}''' = \mathbf{k} + \mathbf{k}']$  may be simultaneously resonant, *i.e.*  $\omega_{\mathbf{k}} \simeq \omega_{\mathbf{k}'} + \omega_{\mathbf{k}''}$  and  $\omega_{\mathbf{k}} \simeq -\omega_{\mathbf{k}'} + \omega_{\mathbf{k}'''}$ . This coupled pair of 3-wave interactions leads to an effective 4-wave interaction involving modes  $\mathbf{k}$ ,  $\mathbf{k}'$ ,  $\mathbf{k}''$  and  $\mathbf{k}'''$ , referred to as the modulational instability mechanism (Gallagher *et al.* 2012).

An important point to emphasize is that, in both the case of the simple resonant 3-wave interaction or the more general modulational instability, resonant coupling between the initial large amplitude (pump) drift mode  $\mathbf{k} = (k_x, k_y \neq 0)$  and a zonal mode  $\mathbf{k}' = (k'_x, k'_y = 0)$  is established via either one sideband  $\mathbf{k}'' = \mathbf{k} - \mathbf{k}'$ , or respectively two sidebands  $\mathbf{k}''$  and  $\mathbf{k}''' = \mathbf{k} + \mathbf{k}'$ , where all these Fourier modes are *linearly decoupled* from each other. As a result, in the situation where in addition to the pump drift mode  $\mathbf{k}$ , the zonal mode  $\mathbf{k}'$  itself already has a finite initial amplitude and a well defined phase, the other daughter waves  $\mathbf{k}''$  (and  $\mathbf{k}'''$ ) are *free* to adapt their phases to ensure a resonant interaction and thus an efficient energy transfer from the pump to the zonal mode, resulting in the further amplification of this zonal mode. In fact, a finite amplitude zonal mode can *stimulate* the decay of multiple non-zonal modes, thus leading to *coherent* (as a result of the frequency matching involved) and therefore *correlated* contributions from these non-zonal modes to the Reynolds stress drive of the zonal mode.

Under realistic conditions, multiple elementary mechanisms such as the ones discussed above (resonant 3-wave interaction / modulational instability) happen both simultaneously and successively in time, leading to an expanding set of Fourier modes, and ultimately to a fully developed turbulent spectrum.

### 5.3. Self-interaction mechanism in sheared toroidal system

As in the shearless slab geometry, in the case of a tokamak system, *i.e.* based on a sheared axisymmetric toroidal magnetic geometry, which is of main interest to our study, the modulational instability involving resonant 3-wave interactions remains an essential driving mechanism of zonal flows (Chen *et al.* 2000). In a tokamak however, one must distinguish another form of the non-linear interaction leading to the drive of zonal modes. This mechanism, referred to as self-interaction, is specific to systems presenting magnetic shear and is explained in the following.

As already discussed in §2, parallel boundary conditions lead to the linear coupling of  $k_x$  Fourier modes. In particular, according to equation (2.13), the electrostatic potential field  $\Phi_L$  of a linear microinstability eigenmode with fixed  $k_{x0}$  and  $k_y \neq 0$  is composed

of Fourier modes  $\hat{\Phi}_{k_{x0}+p\,2\pi k_y\hat{s}, k_y}$ ,  $p \in \mathbb{Z}$ . The spatial dependence of the corresponding eigenmode structure is thus given by:

$$\Phi_L(x, y, z) = \tilde{\Phi}_{k_{x0}, k_y}(x, z) \exp(ik_y y) + \text{c.c.}, \quad (5.6)$$

where c.c. stands for the complex conjugate [considered here to ensure that  $\Phi_L$  is real-valued, essential for computing the quasi-linear estimate in (5.8)], and with the complex-valued  $(x, z)$ -dependent envelope given by:

$$\tilde{\Phi}_{k_{x0}, k_y}(x, z) = \sum_{p=-\infty}^{+\infty} \hat{\Phi}_{k_{x0}+p\,2\pi k_y\hat{s}, k_y}(z) \exp[i(k_{x0} + p\,2\pi k_y\hat{s})x]. \quad (5.7)$$

These linearly coupled  $k_x$  Fourier modes, all having same  $k_y$ , drive the zonal modes  $(k'_x, 0)$ , with  $k'_x = p' \, 2\pi k_y\hat{s}$ ,  $p' \in \mathbb{Z}$ , forming a set of harmonics. Indeed, any two Fourier modes  $\hat{\Phi}_{k_{x0}+p\,2\pi k_y\hat{s}, k_y}$  and  $\hat{\Phi}_{k_{x0}+p''\,2\pi k_y\hat{s}, k_y}$  composing the physical eigenmode will drive, via three Fourier mode coupling, the zonal mode  $\hat{\Phi}_{p'\,2\pi k_y\hat{s}, 0}$  with  $p' = p - p''$  [see equation (5.5)]. Note that this drive of zonal modes is via the same quadratic non-linearity in the gyrokinetic equation related to  $E \times B$  drifts as the one driving zonal modes through the modulational instability, but in this case involving Fourier modes which are already *linearly* coupled to each other.

Assuming that the relative phases between the Fourier modes  $\hat{\Phi}_{k_{x0}+p\,2\pi k_y\hat{s}, k_y}$  remains set by the linear coupling, even during the non-linear turbulent evolution (to what extent this assumption holds is validated in §5.5), the phases of the associated contributions to Reynolds stress driving the zonal modes is *fixed*. This translates in direct space to an essentially fixed periodic radial dependence (with period  $\Delta x_{\text{MRS}} = 1/k_y\hat{s}$  corresponding to the distance between MRSs) of the contribution to Reynolds stress through this self-interaction mechanism from a given  $k_y$  eigenmode, the overall magnitude of this contribution obviously varying in time as the amplitude of the eigenmode evolves. This is a critical difference compared to the drive of zonal modes  $\mathbf{k}'$  through the modulational instability discussed in §5.2, where the relative phases between the pump mode  $\mathbf{k}$  and sidebands  $\mathbf{k}''$ ,  $\mathbf{k}'''$  are *free* to adapt to enable a coherent (*i.e.* in phase) drive of a given zonal mode.

Figure 9 plots the quasi-linear estimates of this self-interaction contribution to the Reynolds stress drive term  $\partial^2 \text{RS} / \partial x^2$  from the linear eigenmode with  $k_{x0} = 0$ ,  $k_y \rho_i = 0.28$ , and  $R/L_{T_i} = 6$ , whose ballooning structures are given in figure 2, considering both the case of kinetic and adiabatic electron response. These results are obtained by inserting the corresponding eigenmode structure (5.6) into relations (5.4) and (5.5), leading to the Reynolds stress contribution denoted  $\widetilde{\text{RS}}_{k_{x0}, k_y}(x)$ :

$$\begin{aligned} \widetilde{\text{RS}}_{k_{x0}, k_y}(x) &= \text{RS}[\Phi_L] = \hat{\text{RS}}_{k_y}[\tilde{\Phi}_{k_{x0}, k_y}] \\ &= 2 \text{Re} \left[ \left\langle \frac{1}{B_0^2} k_y \tilde{\Phi}_{k_{x0}, k_y} \left( g^{xx} i \frac{\partial \tilde{\Phi}_{k_{x0}, k_y}^*}{\partial x} + g^{xy} k_y \tilde{\Phi}_{k_{x0}, k_y}^* \right) \right\rangle_z \right] \\ &= 2 \text{Re} \left[ \sum_{p'=-\infty}^{+\infty} e^{ip'2\pi k_y\hat{s}x} \sum_{p=-\infty}^{+\infty} \left\langle \frac{1}{B_0^2} k_y (g^{xx} k_x'' + g^{xy} k_y) \hat{\Phi}_{k_x, k_y} \hat{\Phi}_{k_x'', k_y}^* \right\rangle_z \right]. \end{aligned} \quad (5.8)$$

In the last equality of relation (5.8),  $k_x = k_{x0} + p\,2\pi k_y\hat{s}$ ,  $k_x'' = k_{x0} + p''\,2\pi k_y\hat{s}$  and  $p'' = p - p'$ . This relation also clearly points out how this contribution to Reynolds stress from a given  $k_y$  eigenmode through self-interaction is periodic with period  $\Delta x_{\text{MRS}} = 1/k_y\hat{s}$ .

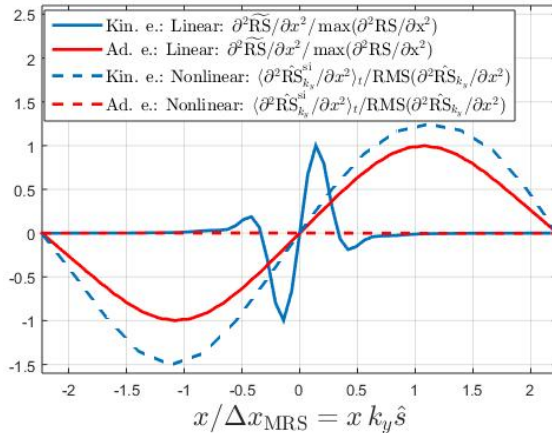


FIGURE 9. Solid lines indicate the quasi-linear estimate of  $\partial^2 \widetilde{RS}_{k_{x0}, k_y} / \partial x^2$  normalised to its maximum value as a function of  $x$  for the linear eigenmode with  $k_{x0} = 0$ ,  $k_y \rho_i = 0.28$  and either kinetic (blue) or adiabatic (red) electrons. Dashed lines denote the time-average  $\langle \partial^2 \widetilde{RS}_{k_y}^{\text{si}} / \partial x^2 \rangle_t$  normalised with respect to the RMS in time of the total contribution  $\partial^2 \hat{RS}_{k_y} / \partial x^2$ , for  $k_y \rho_i = 0.28$ , in turbulence simulations considering either kinetic (blue) or adiabatic (red) electrons.  $k_{y, \min} \rho_i = 0.035$ ,  $R/L_{Ti} = 6$  and other parameters are given in table 1.

The overall amplitude of the quasi-linear estimates shown in figure 9 are naturally irrelevant. Furthermore, as these contributions to Reynolds stress have period  $\Delta x_{\text{MRS}} = 1/k_y \hat{s}$ , only one such period is shown. Note how the radial profile of the quasi-linear estimate of  $\partial^2 \hat{RS}_{k_y} / \partial x^2$  is narrow in the case of kinetic electrons and localized around the MRS at  $x = 0$ , clearly related to the fine structures of the eigenmode at MRSs and the associated broad tail in ballooning representation. As expected, the corresponding radial profile is much broader in the case of adiabatic electrons, as fine structures at MRSs are essentially absent in this case.

#### 5.4. Evidence of zonal flow drive by modulational instability and self-interaction in reduced simulations

In this subsection, we consider reduced non-linear simulation setups in tokamak geometry to clearly illustrate the two basic mechanisms driving zonal flows discussed in §5.2 and §5.3. For these reduced simulations, the same physical parameters as summarized in Table 1 is considered, however with particular initial conditions defined as follows: An unstable linear eigenmode (hereby called the pump mode with  $k_y = k_{y, \text{pump}} \neq 0$ ) is initialized with an amplitude a few times ( $\sim 5$ ) less than the corresponding one in the fully saturated turbulence simulation discussed in §5.5. The purpose of the simulation is to study how this single linear eigenmode drives zonal modes via either the modulational instability or self-interaction. The eigenmode with  $k_{x0} = 0$  and  $k_y \rho_i = 0.28$  was chosen for this pump mode, as it is among the most linearly unstable ones and also contributes significantly to the non-linear fluctuation spectra in the fully developed turbulence simulations (see figures 3 and 7(b)). In addition, zonal Fourier modes (with  $k_y = 0$ ) are initialized to amplitudes 10 – 12 orders of magnitude less than the pump mode to provide a necessary seed for possible modulational instabilities. All Fourier modes not part of the pump and zonal modes are initialized to zero. With this initial setup, only  $k_y$  modes which are harmonics of  $k_{y, \text{pump}}$  can possibly develop non-linearly ( $k_y = p k_{y, \text{pump}}$ ,  $p \in \mathbb{N}$ ). For



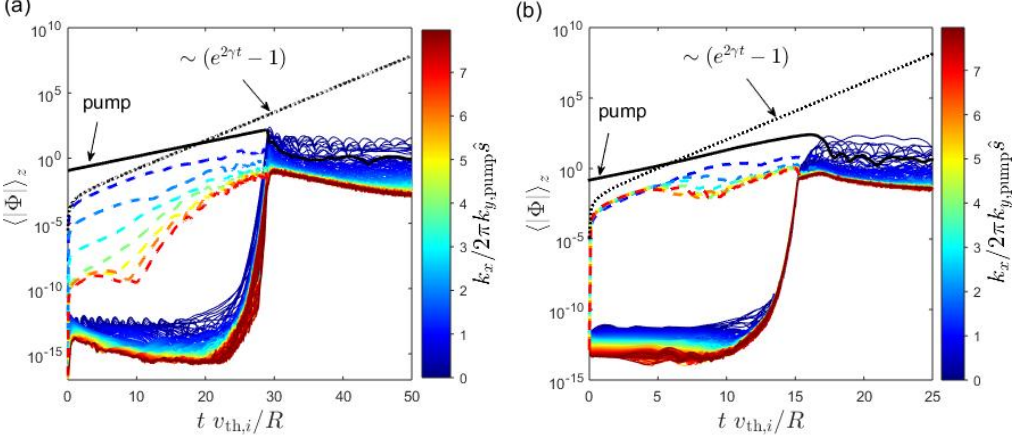


FIGURE 10. Lin-log plots. Coloured lines represent the time evolution of the  $z$ -averaged amplitudes  $\langle |\hat{\Phi}_{k_x, k_y=0}| \rangle_z$  of zonal modes in reduced non-linear simulations initialized with a single large amplitude  $k_{y,pump} \neq 0$  eigenmode, considering either (a) adiabatic or (b) kinetic electrons. The colourbar maps the value of  $k_x$  in units of  $2\pi k_{y,pump} \hat{s}$ . Modes with  $k_x = p' 2\pi k_{y,pump} \hat{s}$ ,  $p' \in \mathbb{N}$ , are plotted with dashed lines. The solid black line represents the time trace of the pump Fourier mode amplitude  $\langle |\hat{\Phi}_{k_x=0, k_{y,pump}}| \rangle_z$ . The dotted black line represents an evolution proportional to  $(e^{2\gamma t} - 1)$ , where  $\gamma$  is the linear growth rate of the pump mode.

these reduced simulations we therefore set  $k_{y,min} = k_{y,pump}$  and actually only considered  $N_{k_y} = 8$  Fourier modes. The flux-tube width in the  $x$  direction was set to  $L_x = M/\hat{s}k_{y,min}$  with  $M = 32$ , so that it remains the same as in full turbulence simulations and the resulting fine  $k_x$ -spectrum allows for a detailed analysis of  $k_x$ -dependence of zonal mode growth. The remaining numerical resolutions are kept the same as in Table 1. This system is then let to evolve until higher  $k_y$  Fourier harmonics start to develop amplitudes similar to the fundamental  $k_{y,pump}$ . These steps ensure that the dominant non-linear interactions mainly involve only  $k_y = 0$  and  $k_{y,pump}$ . This reduced non-linear setup thus clearly isolates the contribution to the drive of zonal modes from a single  $k_y$  mode, while in the much more complex case of a standard fully developed turbulence simulation, multiple  $k_y$  contributions may act simultaneously.

Figure 10 plots the evolution of the pump mode and the zonal modes driven by it. Solid black line represents the time trace of the  $z$ -averaged amplitude of the most dominant Fourier mode  $\langle |\hat{\Phi}_{k_{x0}, k_{y,pump}}| \rangle_z(t)$  composing the pump mode. Note that the other linearly coupled Fourier modes composing the pump mode are not shown. Coloured lines represent the zonal mode amplitude  $\langle |\hat{\Phi}_{k_x, k_y=0}(t)| \rangle_z$  for each  $k_x$ . These results are shown for reduced non-linear simulations considering either adiabatic electrons (figure 10(a)) or kinetic electrons (figure 10(b)).

In the initial stage, the pump eigenmode grows exponentially with corresponding linear growth rates, *i.e.*  $\gamma R/v_{th,i} = 0.25$  in the case of adiabatic electrons and  $\gamma R/v_{th,i} = 0.47$  in the case of kinetic electrons.

Zonal Fourier modes  $\hat{\Phi}_{k'_x, k_y=0}$  with  $k'_x = p' 2\pi k_{y,pump} \hat{s}$ ,  $p' \in \mathbb{Z}$ , (see dashed coloured time traces in figure 10) are driven by the large amplitude pump eigenmode through the self-interaction mechanism, *i.e.* are driven by multiple quadratic non-linearities, each involving two exponentially growing  $k_x$  Fourier components of the pump,  $\hat{\Phi}_{k_x, k_{y,pump}}(t)$ ,  $\hat{\Phi}_{k'_x, k_{y,pump}}(t) \sim e^{\gamma t}$ , where  $k'_x = k_{x0} + p'' 2\pi k_{y,pump} \hat{s}$ ,  $p'' \in \mathbb{Z}$ , and  $p - p'' = p'$ . One

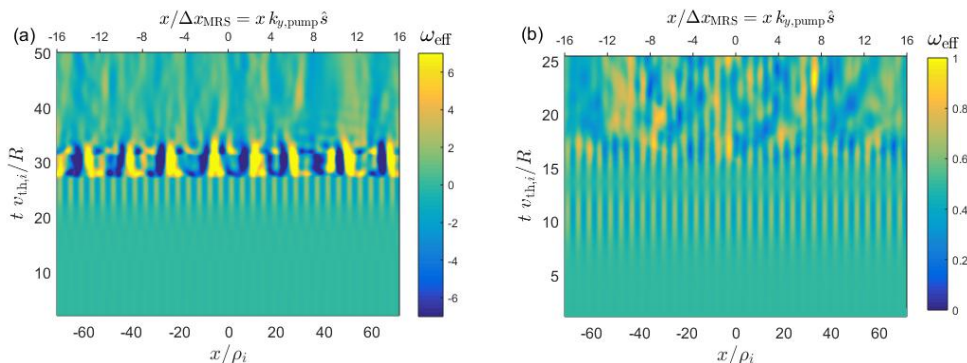


FIGURE 11. Effective zonal flow shearing rate  $\omega_{\text{eff}}$  as a function of radial position  $x$  and time  $t$  for the same reduced non-linear simulations as in figure 10. Cases with either (a) adiabatic or (b) kinetic electrons are shown.

thus has for  $k'_x = p' 2\pi k_{y,\text{pump}} \hat{s}$ :

$$\begin{aligned} \hat{\Phi}_{k'_x, k_y=0}(t) - \hat{\Phi}_{k'_x, k_y=0}(0) &\sim \int_0^t \hat{\Phi}_{k_x, k_{y,\text{pump}}}(t') \hat{\Phi}_{k'_x, k_{y,\text{pump}}}^*(t') dt' \sim \int_0^t e^{2\gamma t'} dt' \\ &\sim (e^{2\gamma t} - 1). \end{aligned}$$

Note that for  $t \ll 1/\gamma$  these modes thus start by growing linearly in time. In the initial stage of the simulations shown in figures 10(a) and 10(b), *i.e.* for  $t \lesssim 28R/v_{\text{th},i}$  and  $t \lesssim 15R/v_{\text{th},i}$  in the case of adiabatic and kinetic electrons respectively, the Fourier modes driven by self-interaction,  $\hat{\Phi}_{p' 2\pi k_{y,\text{pump}} \hat{s}, k_y=0}$ , therefore dominate the zonal  $k_x$ -spectrum. Black dotted lines in these figures indicate the time evolution  $\sim (e^{2\gamma t} - 1)$ , providing a good fit to the initial evolution of these particular zonal modes. As discussed in §5.3, these modes are driven by the Reynolds stress resulting from the self-interaction of the linear eigenmode with  $k_y = k_{y,\text{pump}}$ , which in direct space is periodic in  $x$  with period  $\Delta x_{\text{MRS}} = 1/k_{y,\text{pump}} \hat{s}$  and aligned with corresponding MRSSs. This is clearly reflected in Figures 11(a) and 11(b), plotting the effective zonal flow shearing rate  $\omega_{\text{eff}}$  as a function of  $x$  and time  $t$ , again for simulations with either adiabatic or kinetic electrons. At least in the initial stage of the simulations, these plots indeed present a periodic radial variation of  $\omega_{\text{eff}}$  with period  $1/k_{y,\text{pump}} \hat{s}$  and perfectly aligned with the MRSSs of the pump mode.

Zonal Fourier modes  $\hat{\Phi}_{k'_x, k_y=0}$  with  $k'_x \neq p' 2\pi k_{y,\text{pump}} \hat{s}$ ,  $p' \in \mathbb{Z}$ , (see solid coloured time traces in figure 10) are however driven by the pump eigenmode via the modulational instability mechanism, *i.e.* mainly through the quadratic non-linearities involving the large amplitude Fourier component  $\hat{\Phi}_{k_{x0}, k_{y,\text{pump}}}$  of the pump and either one of the initially low amplitude sideband modes  $\hat{\Phi}_{k_{x0} \pm k'_x, k_{y,\text{pump}}}$ . As a result, these particular zonal modes grow as  $\sim e^{\gamma_{\text{mod}} t}$ , where  $\gamma_{\text{mod}}$  stands for the growth rate of the modulational instability. Given that  $\gamma_{\text{mod}} \sim |\Phi_{\text{pump}}|$  (Hasegawa *et al.* 1979) and that the pump amplitude itself grows exponentially,  $|\Phi_{\text{pump}}| \sim e^{\gamma t}$ , these zonal modes effectively end up growing super-exponentially.

One can also see in figure 10(b) that all plotted zonal modes driven by self-interaction,  $\hat{\Phi}_{p' 2\pi k_{y,\text{pump}} \hat{s}, k_y=0}$ ,  $p' = 1, \dots, 7$ , are from the start driven up to similarly large amplitudes in the case of kinetic electrons, as opposed to the adiabatic case in figure 10(a), where these same modes are driven more weakly. This is explained by the different linear eigenmode structures of the pump in the adiabatic and kinetic electron cases (see corresponding ballooning representations in figure 2). With kinetic electrons, the Fourier

mode components  $\hat{\Phi}_{k_x, k_y, \text{pump}}(z)$ , where  $k_x = k_{x0} + p2\pi k_{y, \text{pump}}\hat{s}$  and  $p \in \mathbb{Z}^*$  (set of integers excluding 0), which compose the tail of the ballooning representation, have much higher relative amplitudes compared to the main Fourier component  $\hat{\Phi}_{k_{x0}, k_y, \text{pump}}(z)$  than in the case with adiabatic electrons. As a result, the self-interaction drive of a zonal mode  $\hat{\Phi}_{p'2\pi k_{y, \text{pump}}\hat{s}, k_y=0}$ ,  $p' \in \mathbb{Z}^*$ , dominated by the non-linear interaction between  $\hat{\Phi}_{k_{x0}, k_y, \text{pump}}(z)$  and  $\hat{\Phi}_{k_{x0}+p'2\pi k_{y, \text{pump}}\hat{s}, k_y, \text{pump}}(z)$ , is stronger with kinetic than with adiabatic electrons.

The weaker drive of the zonal modes by the self-interaction mechanism in the case with adiabatic electrons also explains why these particular zonal modes end up getting overwhelmed by the ones driven by the modulational instability mechanism (reflected by the absence of fine structures at MRSs on  $\omega_{\text{eff}}$  in figure 11(a) for  $t \gtrsim 28 R/v_{\text{th},i}$ ), while they remain significant in the case with kinetic electrons even after saturation of the modes driven by the modulational instability (reflected by the persistent fine structures on  $\omega_{\text{eff}}$  in figure 11(b) even for  $t \gtrsim 15 R/v_{\text{th},i}$ ).

In the following two subsections, evidence of the self-interaction and modulational instability mechanisms are provided in the case of fully developed turbulence simulations, and their relative importance are compared between the cases of adiabatic and kinetic electron responses. Such simulations involve a fully saturated spectra of multiple  $k_y$  modes than the case in the just considered reduced non-linear simulations. We find that the results obtained in the reduced non-linear simulations follow in general to the full turbulence scenarios, but with certain differences.

### 5.5. Evidence of self-interaction in turbulence simulations

In this subsection, the self-interaction mechanism is analysed in fully developed turbulence simulations with physical and numerical parameters given in Table 1. We first test if in this non-linear system, the relative phase differences between the linearly coupled  $k_x$ -Fourier modes remain the same as in corresponding linear eigenmode, as was assumed earlier in §5.3. It is found that the relative phase difference is only partially preserved, and the consequent effect on the Reynolds stress driving zonal flows via self-interaction is illustrated.

To find the non-linear modification of an eigenmode, first the absolute value of the time-averaged ballooning structure of the electrostatic potential  $|\langle \hat{\Phi}_{b, \text{nl}}(\chi, t) / \hat{\Phi}_{b, \text{nl}}(\chi_0 = 0, t) \rangle_t|$  for an eigenmode with  $k_{x0} = 0$  and  $k_y \rho_i = 0.28$  in the full turbulence simulation is plotted along with the corresponding linear ballooning structure  $|\hat{\Phi}_{b, \text{lin}}(\chi) / \hat{\Phi}_{b, \text{lin}}(\chi_0 = 0)|$ , in figure 12(a). See equation (2.15) for the definition of the ballooning structure  $\hat{\Phi}_b(\chi)$ . The non-linear result with kinetic electrons starts significantly deviating from the linear result for  $|\chi| \gtrsim \pi$ . That is, the 'giant tails' in the ballooning structure are reduced compared to the linear case. Nonetheless, the non-linear ballooning structure with kinetic electrons retain more significant tails compared to the case with adiabatic electrons. One also finds that, with kinetic electrons, the relative phase along the ballooning structure  $\delta\phi_{\text{nl}}(\chi, t) = \phi[\hat{\Phi}_{b, \text{nl}}(\chi, t) / \hat{\Phi}_{b, \text{nl}}(\chi_0 = 0, t)]$  remains approximately constant in time (contrary to adiabatic electron results) and equal to its linear value  $\delta\phi_{\text{lin}}(\chi) = \phi[\hat{\Phi}_{b, \text{lin}}(\chi) / \hat{\Phi}_{b, \text{lin}}(\chi_0 = 0)]$ ; Here,  $\phi[A] = \arg(A)$  stands for the phase or argument of the complex number  $A$ . This is true in particular for  $|\chi| \lesssim 4\pi$ , as demonstrated by the solid blue line in figure 12(b) representing  $\Delta\phi(\chi, t) = \delta\phi_{\text{nl}}(\chi, t) - \delta\phi_{\text{lin}}(\chi)$  for  $\chi = 2\pi$  in the kinetic electron case. While there are jumps of  $2\pi$ , the line closely adheres to the linear phase difference. To be quantitative, one considers the estimate  $\text{MOD}(\Delta\phi(\chi, t))$ , where  $\text{MOD}(A) = (|\text{mod}_{2\pi}(A)|^2)_t^{1/2}$ ,  $\text{mod}_{2\pi}(A) \equiv A - 2\pi \times \text{round}(A/2\pi)$ ,  $A \in \mathbb{R}$ , and the function round provides the nearest integer. One notes that, lower the value

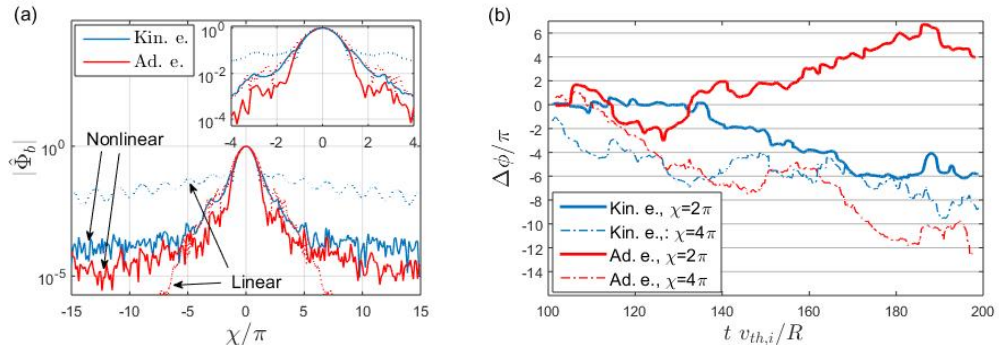


FIGURE 12. (a) Solid lines denote the absolute value of the time-averaged ballooning structure of the electrostatic potential  $|\langle \hat{\Phi}_{b,nl}(\chi, t) / \hat{\Phi}_{b,nl}(\chi_0 = 0, t) \rangle_t|$  for  $k_{x0} = 0$  and  $k_y \rho_i = 0.28$  in the non-linear simulation described in table 1, with  $k_{y,min} \rho_i = 0.035$  and  $R/L_{T,i} = 6$ . Dotted lines denote the corresponding ballooning representation in linear simulations (same as in figure 2). Inset figure shows the zoom near  $\chi = 0$ . Red and blue colours represent adiabatic and kinetic electron simulations respectively. (b) Phase difference  $\Delta\phi(\chi, t) = \phi[(\hat{\Phi}_{b,nl}(\chi, t) / \hat{\Phi}_{b,nl}(\chi_0 = 0, t))(\hat{\Phi}_{b,lin}(\chi_0 = 0) / \hat{\Phi}_{b,lin}(\chi))]$  plotted as a function of time. Here,  $\hat{\Phi}_{b,nl}$  and  $\hat{\Phi}_{b,lin}$  denote the ballooning representation of the electrostatic potential for the same eigenmode considered in subplot (a), in non-linear and linear simulations respectively. Solid and dotted lines represent  $\chi = 2\pi$  and  $4\pi$  respectively.

of  $\text{MOD}(\Delta\phi)$ , more strongly is the relative phase fixed by the linear coupling. Further, for uniform random values of  $\Delta\phi$  between  $-\pi$  and  $\pi$ , one gets  $\text{MOD}(\Delta\phi) = 0.58\pi$ . It is found that, for the case with kinetic electrons,  $\text{MOD}(\Delta\phi(\chi = 2\pi, t)) = 0.34\pi$ . At  $\chi = 4\pi$ , as illustrated by the dotted blue line in figure 12(b), the phase imposed by linear coupling appears to be weakened but still present, giving  $\text{MOD}(\Delta\phi(\chi, t)) = 0.50\pi$ . The corresponding results with adiabatic electrons, denoted by the solid and dashed red lines for  $\chi = 2\pi$  and  $4\pi$  respectively, clearly do not retain constant phase differences. The respective values of  $\text{MOD}(\Delta\phi(\chi, t))$  are  $0.57\pi$  and  $0.61\pi$ .

In other words, in a full turbulence simulation with adiabatic electrons, for a linearly unstable eigenmode with given  $k_{x0}$  and  $k_y$ , linear coupling between the Fourier modes  $(k_x = k_{x0} + 2\pi p k_y \hat{s}, k_y)$  where  $p \in \mathbb{Z}$  have become subdominant compared to non-linear coupling effects. Thus, each  $(k_x, k_y)$  Fourier mode can be considered linearly decoupled as in a shearless slab system and hence, modulational instability is the only driving mechanism of zonal flows in turbulent simulations with adiabatic electrons. On the other hand, with kinetic electrons, for a linearly unstable physical mode with given  $k_{x0}$  and  $k_y$ , linear coupling of Fourier modes is preserved to some extent but reduced to only the three Fourier modes with  $k_x = k_{x0} + 2\pi p k_y \hat{s}$  and  $|p| = 0, \pm 1$ . Only these Fourier modes have their relative phases largely fixed by their linear dynamics (and not for all  $p \in \mathbb{Z}$ , as assumed in §5.3). Hence the self-interaction mechanism is effectively reduced to driving the zonal Fourier modes with  $k'_x = \pm 2\pi k_y \hat{s}$ . Furthermore, the self-interacting contribution to Reynolds stress  $\widetilde{\text{RS}}_{k_{x0}, k_y}(x)$  (defined in equation (5.8)) from the particular physical eigenmode, becomes essentially sinusoidal in  $x$ , spanning the full distance between corresponding MRSs with a period of  $\Delta x_{\text{MRS}} = 1/k_y \hat{s}$ , and with fixed phase/sign in time. Note that the radial width of the fine-structures do not have a dependence on electron-ion mass ratio in turbulence simulations as they are already broadened to span the distance between MRSs as a result of non-linear coupling effects. This is unlike in linear simulations where such a dependence exists (Dominski *et al.* 2015).

The net contribution  $\widehat{\text{RS}}^{\text{si}}$  from the self-interaction mechanism to Reynolds stress can be obtained by summing  $\widehat{\text{RS}}_{k_{x0},k_y}(x)$  over all  $k_y$ 's and all ballooning angles (measured by  $k_{x0}$ ; see (2.16)):

$$\text{RS}^{\text{si}}(x) = \sum_{k_y > 0} \widehat{\text{RS}}_{k_y}^{\text{si}}(x) \quad (5.9)$$

where

$$\widehat{\text{RS}}_{k_y}^{\text{si}} = \sum_{k_{x0} = -\pi k_y \hat{s}}^{\pi k_y \hat{s}} \widehat{\text{RS}}_{k_{x0},k_y}(x). \quad (5.10)$$

In figure 9, the self-interaction contribution  $\partial^2 \text{RS}^{\text{si}} / \partial x^2$  from a particular  $k_y$  in full turbulence simulation is plotted. The dashed lines denote the time average of  $\partial^2 \widehat{\text{RS}}_{k_y}^{\text{si}} / \partial x^2$  for  $k_y \rho_i = 0.28$ , normalised by the RMS in time of total  $\partial^2 \widehat{\text{RS}}_{k_y} / \partial x^2$ , in simulations with kinetic (blue) and adiabatic (red) electrons; the total Reynolds stress contribution  $\widehat{\text{RS}}_{k_y}$  from a given  $k_y$  being defined in (5.5). This diagnostic simultaneously measures the relative importance of self-interaction drive of zonal flows with respect to the total contribution to Reynolds stress drive from the considered  $k_y$ , as well as how good its phase/sign is fixed in time. One notes that, since for a given  $k_y$ , eigenmode with  $k_{x0} = 0$  is the most unstable/dominant, similar results are obtained for  $\widehat{\text{RS}}_{k_{x0}=0,k_y}(x)$  as well, instead of  $\widehat{\text{RS}}_{k_y}^{\text{si}}$  in this diagnostic. From figure 9, one can conclude that, in full turbulence simulations with kinetic electrons, each  $k_y$  contribution  $\partial^2 \widehat{\text{RS}}_{k_y}^{\text{si}} / \partial x^2$  from self-interaction is significant. Furthermore, it is a sinusoidal with a period of  $1/k_y \hat{s}$  and maintains the same sign at each radial position (although with randomly varying amplitude in time, as will be shown at the end of §5.6). In particular,  $\partial^2 \widehat{\text{RS}}_{k_y}^{\text{si}} / \partial x^2$  is zero at MRSs, negative to the left and positive to the right. Whereas with adiabatic electrons, the self-interaction contribution is weak, does not have a fixed sign, and essentially averages out to zero over time. Further, with kinetic electrons, these significant time-averaged self-interaction contributions, localized at MRSs of each  $k_y$ , align at LMRs, driving time-averaged zonal flows at these radial positions. Whereas, away from LMRs, the time-averaged self-interaction contributions  $\partial^2 \widehat{\text{RS}}_{k_y}^{\text{si}} / \partial x^2$  from each  $k_y$  are spatially misaligned and cancel each other out, resulting in relatively negligible time averaged zonal flow levels.

In figure 13, the time average of the total  $\partial^2 \widehat{\text{RS}}_{k_y} / \partial x^2$  is plotted as a function of both position  $x$  and wavenumber  $k_y$ . While between LMRs,  $\partial^2 \widehat{\text{RS}}_{k_y} / \partial x^2$  follows essentially the same spatial orientation (phase) as  $\partial^2 \widehat{\text{RS}}_{k_y}^{\text{si}} / \partial x^2$  in figure 9, near LMRs, there is a reversal of spatial phase. We suspect this to be a result of the back reaction of zonal modes driven by self-interaction on turbulence. At the moment, we postpone further analysis on this to a later time.

Recall from earlier in this subsection that in kinetic electron turbulence simulations, the self-interaction contribution from a given  $k_y \neq 0$  is effectively reduced to driving the zonal Fourier modes with  $k'_x = \pm 2\pi k_y \hat{s}$ . The combined self-interacting contributions from the various  $k_y$ 's therefore drive zonal Fourier modes with  $k_x = 2\pi p \hat{s} k_{y,\min}$ , where  $p \in \mathbb{Z}$ . This can be seen as peaks in the  $k_x$ -spectra of the time-averaged shearing rate  $\langle \omega_{\text{eff}} \rangle_t$ , shown with blue dashed line in figure 14 and correspond to the time-constant structures at LMRs separated by  $\Delta x_{\text{LMRS}} = 1/\hat{s} k_{y,\min}$  in figure 5. Given that, in the case of the reference turbulence simulation with kinetic electrons, the highest contribution to heat flux (see figure 7(b)) and the  $|\Phi|^2$  amplitude spectra is at  $k_y \rho_i \sim 0.21$  and that for a given  $k_y$ , eigenmodes with  $k_{x0} = 0$  are the most dominant, the zonal mode with

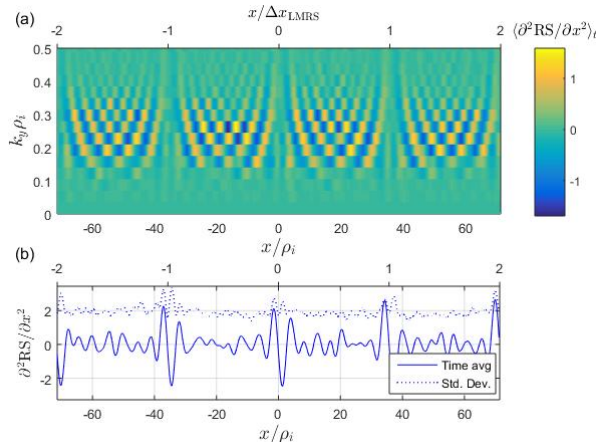


FIGURE 13. (a) Each  $k_y$  contribution of  $\langle \partial^2 \text{RS} / \partial x^2 \rangle_t$  plotted as a function of the radial coordinate  $x$ . (b) Total  $\langle \partial^2 \text{RS} / \partial x^2 \rangle_t$  plotted vs  $x$ . Dashed line denote the standard deviation. Results correspond to the non-linear simulation described in table 1, with  $k_{y,\min} \rho_i = 0.035$ ,  $R/L_{T,i} = 6$  and kinetic electrons.

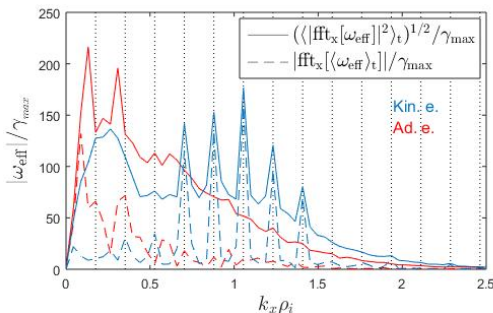


FIGURE 14.  $k_x$  spectra of the effective shearing rate  $\omega_{\text{eff}}$  in turbulence simulations with adiabatic (red) and kinetic (blue) electrons. Corresponding parameters are given in table 1, with  $k_{y,\min} \rho_i = 0.035$  and  $R/L_{T,i} = 6$ . Solid lines and dashed lines represent time average of the amplitude and amplitude of the time average of  $\omega_{\text{eff}}$  respectively. All traces are normalised by corresponding maximum linear growth rate  $\gamma_{\text{max}}$ . Vertical dotted lines indicate positions where  $k_x = 2\pi p \delta k_{y,\min}$ ;  $p \in \mathbb{Z}$ .

$k_x \rho_i \sim 2\pi \hat{s} \times 0.21 \sim 1.06$  are driven strongly via the self-interaction mechanism and hence has the highest value in the  $k_x$ -spectra of shearing rate. Similarly, those  $k_y$ 's with lower heat flux and amplitude contributions, contribute lesser towards the self-interaction mechanism and thereby explains the number and position of peaks in the  $k_x$ -spectra of shearing rate with kinetic electrons in figure 14.

Solid red line in figure 14 denotes the  $k_x$ -spectra of  $\omega_{\text{eff}}$  in the simulation with adiabatic electron response. These zonal Fourier modes are driven predominantly by modulational instability. In the next subsection, we test, if consequently, as a result of the frequency matching involved in the modulational instability mechanism, those zonal modes having high shearing rate amplitudes end up playing a major role in pacing the dynamics of much of the  $(k_x, k_y \neq 0)$  Fourier modes in adiabatic electron simulations.

### 5.6. Evidence of modulational instability in turbulence simulations. Bicoherence and correlation analysis.

In this subsection, we verify in fully developed turbulence simulations, that indeed with adiabatic electron response, zonal flows are driven predominantly via modulational instability, as found in reduced simulations in §5.4 and as discussed in §5.5. We test this by doing a bicoherence-like analysis. We simultaneously show that, as a consequence, this leads to *correlated* contributions from the various  $k_y$ 's to the Reynolds stress drive of zonal modes. We furthermore show that in kinetic electron simulations, the self-interaction contributions to Reynolds stress from the various  $k_y$ 's are random in time and *decorrelated* with each other.

As already discussed earlier, modulational instability mechanism involves resonant 3-wave interactions which require frequency matching. The strength of a particular resonant interaction between the 3 Fourier modes,  $\mathbf{k} = (k_x, k_y)$ , the zonal mode  $\mathbf{k}' = (k'_x, 0)$  and daughter mode  $\mathbf{k}'' = \mathbf{k} - \mathbf{k}' = (k_x - k'_x, k_y)$ , can thus be measured via a bicoherence-type analysis, essentially involving the time-average of the triplet product

$$T(\mathbf{k} ; +\mathbf{k}') = \hat{\Phi}_{\mathbf{k}}(t)\hat{\Phi}_{\mathbf{k}'}^*(t)\hat{\Phi}_{\mathbf{k}''}^*(t) \quad (5.11)$$

where  $\hat{\Phi}_{\mathbf{q}}(t) \sim \exp[-i(\omega_{\mathbf{q}}t + \phi_{\mathbf{q}})]$  is the complex time dependent amplitude of the electrostatic field with any Fourier mode  $\mathbf{q}$ , having a frequency  $\omega_{\mathbf{q}}$ , initial phase  $\phi_{\mathbf{q}}$ , and evaluated at  $z=0$ . If the Fourier modes  $[\mathbf{k}, \mathbf{k}', \mathbf{k}'' = \mathbf{k} - \mathbf{k}']$  are frequency matched in the simulation time, i.e.  $\omega_{\mathbf{k}} = \omega_{\mathbf{k}'} + \omega_{\mathbf{k}''}$ , then  $\langle T(\mathbf{k} ; +\mathbf{k}') \rangle_t \neq 0$ , where  $\langle \cdot \rangle_t$  stands for the time-average over the simulation time.

Here, we remark that, for a given set of Fourier modes  $[\mathbf{k}, \mathbf{k}', \mathbf{k}'' = \mathbf{k} - \mathbf{k}']$  under frequency matching condition, different resonant decay mechanisms could be possible, each with a specific phase difference  $\Delta\phi = \phi_{\mathbf{k}} - \phi_{\mathbf{k}'} - \phi_{\mathbf{k}''}$  associated to it. Hence, a non-zero time average  $\langle T(\mathbf{k} ; +\mathbf{k}') \rangle_t$  over the simulation time is indicative of a particular resonant decay mechanism being persistent throughout the simulation.

Now, a normalised measure of the strength of the resonant 3-wave interaction can be calculated by the following estimate:

$$b_N(\mathbf{k} ; +\mathbf{k}') = \frac{|\langle T(\mathbf{k} ; +\mathbf{k}') \rangle_t|}{\langle |T(\mathbf{k} ; +\mathbf{k}')| \rangle_t}, \quad (5.12)$$

defined as the bicoherence between the Fourier triplet  $[\mathbf{k}, \mathbf{k}', \mathbf{k}'' = \mathbf{k} - \mathbf{k}']$ . Note  $0 \leq b_N \leq 1$ . Further,  $b_N(\mathbf{k} ; +\mathbf{k}') \simeq 1$  indicates a fully resonant 3-wave interaction between  $\mathbf{k}$ ,  $\mathbf{k}''$  and the zonal mode  $\mathbf{k}'$ , while  $b_N \simeq 0$  indicates a non-resonant process. Since modulational instability is a simultaneous resonant interaction between both triplets  $[\mathbf{k}, \mathbf{k}', \mathbf{k}'' = \mathbf{k} - \mathbf{k}']$  and  $[\mathbf{k}, -\mathbf{k}', \mathbf{k}''' = \mathbf{k} + \mathbf{k}']$ , we define total bicoherence

$$B_N(\mathbf{k} ; \mathbf{k}') = (b_N(\mathbf{k} ; +\mathbf{k}') + b_N(\mathbf{k} ; -\mathbf{k}'))/2, \quad (5.13)$$

such that a value of  $B_N \simeq 1$  indicates a fully resonant modulational instability mechanism. In general, values of  $B_N$  closer to zero are indicative of non-resonant interactions while larger values of  $B_N$  are characteristic of modulational instability mechanisms.

Figure 15(a) shows  $B_N(\mathbf{k} ; \mathbf{k}')$  as a function of  $\mathbf{k} = (k_x, k_y)$ , in the reference simulation with adiabatic electrons, for the fixed zonal mode with  $\mathbf{k}' = (k'_x = 0.13\rho_i^{-1}, 0)$  which has the highest contribution to the zonal shearing rate  $k_x$ -spectra (see solid red line in figure 14). One can see that most  $\mathbf{k} = (k_x, k_y)$  have high values of  $B_N \gtrsim 0.3$ , reflecting the dominance of resonant 3-wave interaction processes. Whereas in figure 15(b), corresponding kinetic electron simulation result for the zonal mode with  $\mathbf{k}' = (k'_x = 0.26\rho_i^{-1}, 0)$  having highest contribution to the shearing rate  $k_x$ -spectra shows much smaller values



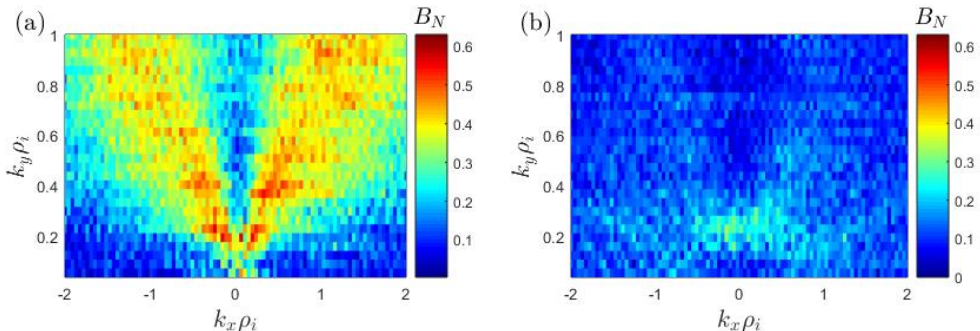


FIGURE 15. The bicoherence level  $B_N$ , as defined by equation (5.13), in (a) adiabatic and (b) kinetic electron turbulence simulations, for the zonal modes with  $k'_x \rho_i = 0.13$  and  $0.26$  respectively. Results correspond to simulations with parameters as given in table 1, with  $k_{y,\min} \rho_i = 0.035$  and  $R/LT_i = 6$ .

of  $B_N$ , indicating much weaker resonant 3-wave interactions. Similar differences are seen between adiabatic and kinetic electron results for other zonal modes  $\mathbf{k}' = (k'_x, 0)$  as well.

Note that, for a given zonal mode  $\mathbf{k}' = (k'_x, 0)$ , under wave vector matching condition, one has the following approximate estimate between associated triple products and the Reynolds stress contributions driving the particular zonal mode:

$$\sum_{k_x} T(\mathbf{k}; \mathbf{k}') \sim \hat{\Phi}_{\mathbf{k}'}^* \hat{\text{RS}}_{k_y}, \quad (5.14)$$

where  $\hat{\text{RS}}_{k_y}$  has been defined in equation (5.5). Now, if  $\langle T(\mathbf{k}; \mathbf{k}') \rangle_t$  (and the corresponding total bicoherence  $B_N(\mathbf{k}; \mathbf{k}')$ ) for multiple Fourier modes  $\mathbf{k} = (k_x, k_y)$  are simultaneously significant for the same dominant zonal mode  $\mathbf{k}'$  (as is the case in figure 15(a) for adiabatic electron simulation), then based on (5.14) one can conclude that the Reynolds stress contributions  $\hat{\text{RS}}_{k_y}$  from the various  $k_y$ 's tend to be in phase with the particular zonal mode. This implies a coherent and thus correlated contributions (drives) from these various  $\hat{\text{RS}}_{k_y}$  ( $\partial^2 \hat{\text{RS}}_{k_y} / \partial x^2$ ). To verify this explicitly, we define an effective correlation function  $C_{\text{RS}}$  measuring the average correlation between all pairs of  $[\partial^2 \hat{\text{RS}}_{k_{y,1}} / \partial x^2, \partial^2 \hat{\text{RS}}_{k_{y,2}} / \partial x^2]$  for  $k_{y,1} \neq k_{y,2}$ :

$$C_{\text{RS}}[f] = \sum_{\substack{k_{y,i}, k_{y,j} \\ k_{y,j} > k_{y,i}}} \frac{\text{Cov}[\hat{f}_{k_{y,i}}, \hat{f}_{k_{y,j}}]}{\sigma[\hat{f}_{k_{y,i}}] \sigma[\hat{f}_{k_{y,j}}]} \bigg/ \sum_{\substack{k_{y,i}, k_{y,j} \\ k_{y,j} > k_{y,i}}} 1. \quad (5.15)$$

$f = \partial^2 \text{RS} / \partial x^2$ ,  $\hat{f}_{k_y} = \partial^2 \hat{\text{RS}}_{k_y}(x) / \partial x^2$ , covariance  $\text{Cov}[a, b] = (\sigma^2[a + b] - \sigma^2[a] - \sigma^2[b]) / 2$ , and variance  $\sigma^2[a] = \langle |a - \langle a \rangle_t|^2 \rangle_t$ , with  $\langle \cdot \rangle_t$  representing average over simulation time. Note that  $C_{\text{RS}} \in [0, 1]$ , with 1 corresponding to perfect correlation between Reynolds stress drive from all  $k_y$ 's and 0 corresponding to total decorrelation between them. In figure 16,  $C_{\text{RS}}$  is plotted as a function of the radial position  $x$ , for adiabatic and kinetic electron turbulence simulations. We can find that  $C_{\text{RS}}[\partial^2 \text{RS} / \partial x^2]$  for adiabatic electron case (solid red line) only shows  $\sim 7\%$  correlation. However the important point to note is that this is roughly an order of magnitude higher than that for kinetic electron simulation (solid blue line). Thus, this diagnostic verifies that in adiabatic electron turbulence simulations where modulational instability mechanism is stronger, Reynolds stress drive  $\partial^2 \hat{\text{RS}}_{k_y} / \partial x^2$  from the various  $k_y$ 's are indeed more correlated with each other, when



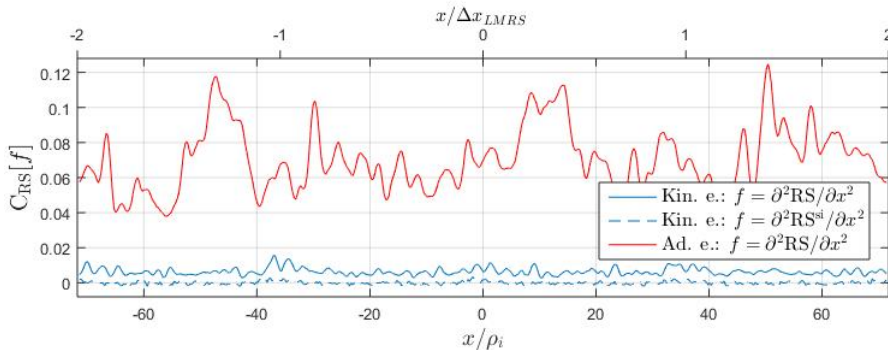


FIGURE 16. Correlation between the  $k_y$  modes of  $\partial^2 \text{RS}/\partial x^2$ , as defined by equation (5.15), as a function of  $x$  in turbulence simulations with kinetic (solid blue line) and adiabatic (solid red line) electrons. Corresponding parameters are given in table 1, with  $k_{y,\min} \rho_i = 0.035$  and  $R/L_{T,i} = 6$ . Correlation between the  $k_y$  modes of self-interacting contribution  $\partial^2 \text{RS}^{\text{si}}/\partial x^2$  in the simulation with kinetic electrons is shown with dashed blue line.

compared to kinetic electron simulations where modulational instability mechanism is weaker.

The same correlation diagnostic is now performed on the self-interacting part of Reynolds stress in kinetic electron simulations. In figure 16, the correlation between the  $k_y$  contributions to  $\partial^2 \text{RS}^{\text{si}}/\partial x^2$ , measured by  $C_{\text{RS}}[\partial^2 \text{RS}^{\text{si}}/\partial x^2]$ , is found to be nearly zero. This implies that, each  $k_y$  contribution to  $\partial^2 \text{RS}^{\text{si}}/\partial x^2$  at a given radial position (while in general having a fixed sign) has an amplitude that is completely independent and decorrelated with each other. The self-interaction drive of zonal modes from each  $k_y$  thus acts like random kicks. Consequently, if the decorrelated (*incoherent*) contributions from the self-interaction mechanism becomes significant, it may disrupt the (*coherent*) modulational instability interactions. We interpret this as being the cause for lower bicoherence values of  $B_N$  in figure 15(b), as well as the lower level of  $C_{\text{RS}}[\partial^2 \text{RS}/\partial x^2]$  in figure 16 with kinetic electrons as compared to adiabatic electrons.

To summarise, in this section 5, the two different mechanisms driving zonal flows, namely modulational instability and self-interaction, have been discussed in detail. We have shown that, as a result of the stronger linear  $k_x$ -couplings within an eigenmode in kinetic electron simulations, the associated drive of zonal flows via self-interaction is much more significant, than in the case of adiabatic electron simulations. This has been illustrated in both reduced and full turbulence simulations. Furthermore, in turbulence simulations, it was shown that the contributions to zonal flow drive from each  $k_y$  mode, via the self-interaction mechanism, are random and decorrelated with each other in time. In the next section, we explain how such a decorrelated drive can lead to a decrease in the fluctuating zonal flow levels with decreasing  $k_{y,\min} \rho_i$ .

## 6. Estimating the reduction in zonal flow drive from self-interaction with decreasing $k_{y,\min} \rho_i$

The low temporal correlation between the various  $k_y$  contributions to the Reynolds stress drive  $\partial^2 \text{RS}/\partial x^2$  of zonal flows in kinetic electron simulations, which is a result of strong self-interaction mechanism, could explain the decrease in the level of shearing rate  $\omega_{\text{eff}}$  associated to fluctuating  $E \times B$  zonal flows with increasing toroidal system size,

over the range of  $k_{y,\min}\rho_i$  considered in figure 6(c). This explanation is based on simple statistical arguments described as follows.

To start with, let us assume that the fluctuation energy density, proportional to amplitude density  $|\Phi|^2$  of the fluctuating electrostatic field  $\Phi$ , remains the same across the simulations with different  $k_{y,\min}$ s. Consequently the amplitude  $|\hat{\Phi}_{k_y}|^2$  of each  $k_y$  Fourier component of the electrostatic field scales as  $1/N_y$  where  $N_y$  is the number of participating modes, according to the following estimate based on Parseval's identity:

$$\frac{1}{L_y} \int_0^{L_y} |\Phi|^2 dy = \sum_{k_y=0}^{N_y} |\hat{\Phi}_{k_y}|^2 = \text{constant} \implies |\hat{\Phi}_{k_y}|^2 \sim \frac{1}{N_y}. \quad (6.1)$$

Here,  $\hat{\Phi}_{k_y}$  is defined as per the relation

$$\Phi(x, y, z) = \sum_{k_y} \hat{\Phi}_{k_y}(x, z) e^{ik_y y}. \quad (6.2)$$

Since Reynolds stress is a quadratic quantity in  $\Phi$ , the scaling in relation 6.1 also implies that each  $k_y$  contribution to the Reynolds stress drive scales as  $\partial^2 \hat{\text{RS}}_{k_y} / \partial x^2 \sim |\hat{\Phi}_{k_y}|^2 \sim 1/N_y$ . Since  $N_y = k_{y,\max}/k_{y,\min}$  and  $k_{y,\max}$  remains the same across simulations in the  $k_{y,\min}$  scan, one also has  $1/N_y \sim k_{y,\min}$ .

Now, further assuming the various  $k_y$  contributions to Reynolds stress drive  $\partial^2 \hat{\text{RS}}_{k_y} / \partial x^2$  to be nearly fully decorrelated (characteristic of kinetic electron simulations; see figure 16), the variance of the total Reynolds stress drive  $\partial^2 \text{RS} / \partial x^2 = \sum_{k_y} \partial^2 \hat{\text{RS}}_{k_y} / \partial x^2$  becomes the sum of variances of all  $k_y$  contributions:

$$\text{Var} \left( \sum_{k_y} \frac{\partial^2}{\partial x^2} \hat{\text{RS}}_{k_y} \right) \simeq \sum_{k_y} \text{Var} \left( \frac{\partial^2}{\partial x^2} \hat{\text{RS}}_{k_y} \right) \sim N_y \frac{1}{N_y^2} \sim \frac{1}{N_y} \sim k_{y,\min}, \quad (6.3)$$

having made use of  $\text{Var}(\partial^2 \hat{\text{RS}}_{k_y} / \partial x^2) \sim 1/N_y^2$ , given that  $\partial^2 \hat{\text{RS}}_{k_y} / \partial x^2 \sim 1/N_y^2$ . We therefore expect the standard deviation SD of the Reynolds stress drive  $\partial^2 \text{RS} / \partial x^2$  to scale as  $\text{SD} = \text{Var}^{0.5} \sim k_{y,\min}^{0.5}$ . Further, since  $\partial^2 \text{RS} / \partial x^2$  is a proxy for the drive of zonal flows, this explains a decrease in the standard deviation of  $\omega_{\text{eff}}$  with decreasing  $k_{y,\min}$ .

From the  $k_{y,\min}$  scan performed with kinetic electrons,  $R/L_{T,i} = 6$  and other parameters as given in Table 1, we find that the x and time-averaged standard deviation  $\langle \text{SD}(\partial^2 \text{RS} / \partial x^2) \rangle_{x,t}$  of the Reynolds stress drive actually scales as  $k_{y,\min}^{0.22}$ , as shown in figure 17. This mismatch between the expected and observed scalings pushes us to reconsider the assumptions made that led to the estimate  $\text{SD} \sim k_{y,\min}^{0.5}$ .

The small but non-zero value of the correlation between the  $k_y$  contributions of  $\partial^2 \text{RS} / \partial x^2$  in these simulations (see solid blue line in figure 16) may account for a small part of the discrepancy. However, the primary cause seems to arise from the faulty assumption of constant fluctuation energy density across simulations with different  $k_{y,\min}$ s. As the zonal flow shearing rate decreases with decreasing  $k_{y,\min}$ , the energy density in the system tends to increase, so that the estimate made in relation 6.1 has to be reconsidered. This is confirmed in figure 17 where the same set of simulations show  $\langle |\hat{\Phi}_{k_y}|^2 \rangle_{x,z,t} \sim k_{y,\min}^{0.73}$ , for  $k_y \rho_i = 0.28$  having a significant amplitude in the  $k_y$ -spectra of  $|\Phi|^2$  and heat flux. Using this scaling  $\partial^2 \hat{\text{RS}}_{k_y} / \partial x^2 \sim |\hat{\Phi}_{k_y}|^2 \sim k_{y,\min}^{0.73}$  in place of  $\sim k_{y,\min}^1$

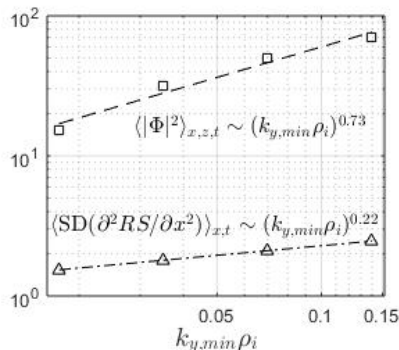


FIGURE 17. Triangles: Standard deviation  $\langle SD(\partial^2 RS / \partial x^2) \rangle_{x,t}$  of Reynolds stress drive plotted as a function of  $k_{y,min}$  in log-log scale, in turbulence simulations with kinetic electrons. Corresponding parameters are given in table 1, with  $R/L_{T,i} = 6$ . Fit (dashed-dotted line) shows scaling  $\sim (k_{y,min} \rho_i)^{0.22}$ . Squares:  $\langle |\hat{\Phi}|^2 \rangle_{x,z,t}$  ( $k_y \rho_i = 0.28$ ) plotted as a function of  $k_{y,min}$ , in the same set of simulations. Fit (dashed line) shows scaling  $\sim (k_{y,min} \rho_i)^{0.73}$ .

in (6.3), we get

$$\text{Var} \left( \sum_{k_y} \frac{\partial^2}{\partial x^2} \hat{RS}_{k_y} \right) \simeq \sum_{k_y} \text{Var} \left( \frac{\partial^2}{\partial x^2} \hat{RS}_{k_y} \right) \sim \frac{1}{k_{y,min}} (k_{y,min}^{0.73})^2 \sim k_{y,min}^{0.46}, \quad (6.4)$$

*i.e.* the standard deviation of  $\partial^2 RS / \partial x^2$  scales as  $SD = \text{Var}^{0.5} \sim k_{y,min}^{0.23}$ , which is very close to the observed trend of  $\langle SD(\partial^2 RS / \partial x^2) \rangle_{x,t} \sim k_{y,min}^{0.22}$ .

## 7. Conclusions

In this paper, we have addressed the self-interaction mechanism and how it affects the drive of zonal flows in ion-scale gyrokinetic turbulence simulations. The basic mechanism of self-interaction is the process by which a microinstability eigenmode non-linearly interacts with itself, generating a Reynolds stress contribution localised at its corresponding MRS (figure 9). Compared to adiabatic electron simulations, this effect is more prominent in kinetic electron simulations. The origin of this increased self-interaction in kinetic electron simulations is the result of the non-adiabatic passing electron response at MRSs leading to fine slab-like structures at these radial positions, reflected as well by broadened ballooning structures of the eigenmodes (figure 2).

These self-interacting contributions from various eigenmodes to Reynolds stress radially align at low order MRSs to generate significant stationary zonal flow shear layers at these positions. However, given that low order MRSs occupy only a tiny radial fraction of core tokamak plasmas, we have focused primarily on how self-interaction affects the drive of zonal flows between the low order MRSs. We have found that self-interaction plays an important role in generating fluctuating zonal flows, in fact *throughout* the full radial extent. These fluctuating components of zonal flows are furthermore found to be critical to regulating transport levels.

These findings were obtained by studying the self-interaction contributions to Reynolds stress drive from the various microturbulence modes by focusing on their statistical properties. Critical to this approach has been to vary the number of significant toroidal modes participating in our turbulence simulations by performing scans over  $k_{y,min} \rho_i$ .

In these turbulence simulations, using correlation analysis (see figure 16), we have

in particular shown that the amplitude of the Reynolds stress contributions from self-interaction of each microturbulence mode are essentially random and decorrelated with each other. In the case of kinetic electron simulations, the significant self-interaction mechanism can in this way disrupt the coherent contributions from the alternative zonal flow drive process provided by the modulational instability mechanism, as reflected by the corresponding weak bicoherence analysis estimates presented in figure 15. In simulations with adiabatic electrons however, for which self-interaction is weak, bicoherence estimates reflect strong resonant 3 wave interactions, characteristic of the modulational instability process being dominant in this case.

Using simple statistical scaling arguments we have then demonstrated how such a decorrelated drive from the self-interaction of various microturbulence modes could in turn lead to a decrease in shearing rate associated to fluctuating zonal flows with decreasing  $k_{y,\min}\rho_i$  [see kinetic electron results in figure 6(c)]. Assuming that the zonal flow shearing mechanism is the dominant saturation mechanism at play, this in turn would lead to an increase in gyro-Bohm normalised heat and particle flux levels as  $k_{y,\min}\rho_i$  decreases.

For the range  $k_{y,\min}\rho_i = 10^{-2} - 10^{-1}$  considered in section 4, the kinetic electron simulations far from marginal stability [blue circles in figure 7(a)] indeed show such an increase in ion heat flux, presenting a power law scaling of the form  $(k_{y,\min}\rho_i)^\alpha$ , with  $\alpha < 0$ . It is important to note that, as one continues to decrease  $k_{y,\min}\rho_i$ , this scaling ultimately breaks and the simulation results do finally converge; in other words, the true  $\rho^* \rightarrow 0$  limit of the flux-tube model can be reached, as already reported in the work by Ball *et al.* (2020). To demonstrate this for the particular case far from marginal stability ( $R/L_{T,i} = 6$ ), the original scan was extended to lower values of  $k_{y,\min}\rho_i$ , but with a quarter of the resolution in the radial direction to make the runs computationally feasible. The corresponding ion heat flux plot is shown in figure 18(a), where the power law scaling finally breaks for  $k_{y,\min}\rho_i \lesssim 10^{-2}$ , and a convergence within 5% is observed at  $k_{y,\min}\rho_i \sim 5 \times 10^{-3}$ . The corresponding estimates of the effective shearing rate, namely  $\text{RMS}_{x,t}(\omega_{\text{eff}})$ ,  $\text{SD}_{x,t}(\omega_{\text{eff}})$  and  $\text{RMS}_x(\langle \omega_{\text{eff}} \rangle_t)$ , are plotted in figure 18(b). As had been discussed in §4, the most interesting quantity to us is the shearing rate of fluctuating zonal flows measured by  $\text{SD}_{x,t}(\omega_{\text{eff}})$ , which is also seen to deviate from its the power law scaling for values of  $k_{y,\min}\rho_i \lesssim 10^{-2}$ , hinting towards a near convergence for  $k_{y,\min}\rho_i \sim 5 \times 10^{-3}$ . Furthermore, in figure 8, corresponding results of the radial correlation length of turbulent eddies is given, also showing a convergence for  $k_{y,\min}\rho_i \sim 5 \times 10^{-3}$ .

Closer to marginal stability [green line in figure 7(a)], the gyro-Bohm normalised flux levels in kinetic electrons simulations appear to be already essentially converged for  $k_{y,\min}\rho_i \sim 10^{-2}$ . The convergence of fluxes observed for this particular case is despite a decrease in the shearing rate associated to zonal flows (seen in  $\text{RMS}_{x,t}(\omega_{\text{eff}})$ ,  $\text{SD}_{x,t}(\omega_{\text{eff}})$  and  $\text{RMS}_x(\langle \omega_{\text{eff}} \rangle_t)$ , shown with green lines in figure 6(a-c)). One possible explanation for this could be that, as the various estimates of normalised shearing rate decrease below  $\omega_{\text{eff}}/\gamma_{\text{max}} \simeq 1$ , the zonal flow saturation mechanism becomes less effective in regulating flux levels. Other saturation mechanisms such as that via damped eigenmodes (Hatch *et al.* 2011) could then be taking over.

Since  $k_{y,\min}\rho_i \sim \rho^*$ , one can interpret the decrease in zonal flow shearing rates and the possible associated increase in heat and particle flux levels in any particular range in  $k_{y,\min}\rho_i$  as a finite toroidal system size effect still present in the flux-tube simulations. One may deal in practice with this system size dependence of flux-tube simulations in two ways:

1. One approach has the intent of correctly resolving this physical finite  $\rho^*$  effect, but to be accurate, this requires considering the physical  $k_{y,\min}\rho_i = n_{\min}(q_0 a/r_0)\rho^*$  value

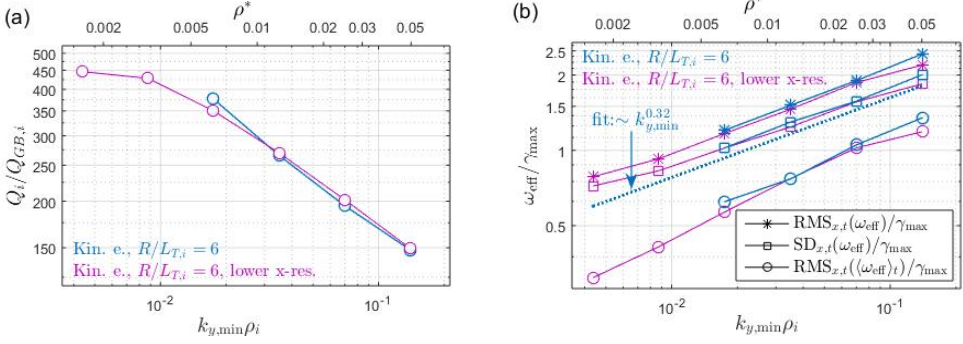


FIGURE 18. (a) Ion heat flux plotted as a function of  $k_{y,min} \rho_i$ . (b) Asterisks, squares and circles represent  $\text{RMS}_{x,t}(\omega_{\text{eff}})$ ,  $\text{SD}_{x,t}(\omega_{\text{eff}})$  and  $\text{RMS}_{x,t}(\langle \omega_{\text{eff}} \rangle_t)$  respectively, plotted as a function of  $k_{y,min} \rho_i$ . In both sub-plots, blue colour represents the kinetic electron reference simulations whose parameters are given in table 1 [the case far from marginal stability ( $R/L_{T,i} = 6$ )]; these are the same plots as those shown with blue colour in figure 7(a) and figure 6. Magenta colour represent simulations with a quarter of the resolution in the radial coordinate.

of the tokamak plasma conditions one is studying, which corresponds to the flux-tube covering the *full* reference flux-surface in both the poloidal (with  $L_z = 2\pi$ ) and toroidal (with  $n_{\min} = 1$ ) directions. In this paper, only this approach has been considered.

This can however be quite challenging in practice, even for flux-tube simulations relevant for a medium-sized tokamak. A scan in  $k_{y,min}$ , even when limited to ion scale turbulence, is numerically quite costly, as it involves computations of larger and larger systems along  $y$  as  $k_{y,min}$  is decreased. For DIII-D for example, with  $\rho^* \simeq 1/300$ , for a full flux-surface located at mid-radius of the plasma ( $r_0/a = 0.5$ ), for  $q_0 = 1.4$  considered here, the value of  $k_{y,min} \rho_i = (q_0 a / r_0) \rho^* \simeq 1.4 \cdot 10^{-2}$  is approximately equal to the value  $k_{y,min} \rho_i = 0.0175$  considered in our scan. Large machines such as JET ( $\rho^* \simeq 1/600$ ) and ITER ( $\rho^* \simeq 1/1000$ ) has corresponding values of  $k_{y,min} \rho_i \simeq 4.7 \cdot 10^{-3}$  and  $2.8 \cdot 10^{-3}$  respectively.

Therefore in practice, if the simulation results (including heat and particle fluxes, shearing rate associated to zonal flows, radial correlation length of turbulent eddies etc.) are found to be converged for values of  $k_{y,min} \rho_i$  larger than that corresponding to the machine one is interested in, then one obviously does not need to simulate the full physical flux-surface, as the system size effect of self-interaction has also saturated. However, if no such convergence is observed as  $k_{y,min} \rho_i$  approaches the physical value corresponding to the machine, then one should use that physical  $k_{y,min} \rho_i$  and correctly account for the effect of self-interaction (Ball *et al.* 2020).

Note that, with this approach of using flux-tube simulations to physically resolve the particular finite system size effect resulting from the self-interaction mechanism, the other finite  $\rho^*$  effects, such as profile shearing (Waltz *et al.* 1998, 2002), effect of finite radial extent of the unstable region (McMillan *et al.* 2010) etc., are missing. Therefore, if one wants to study how self-interaction competes with other finite  $\rho^*$  effects, either *global* simulations should be used, or local simulations that treat these other finite  $\rho^*$  effects explicitly such as (Candy *et al.* 2020). Note that even in global simulations, the full flux-surface will have to be modelled to accurately account for self-interaction, in the sense that a simulation volume covering only a toroidal wedge, corresponding to considering  $n_{\min} > 1$ , is in general insufficient.

2. As a second approach, one can deliberately remove the effects of self-interaction, as suggested by Beer *et al.* (1995); Faber *et al.* (2018); Ball *et al.* (2020), by increasing the parallel length of the simulation volume along the magnetic field until convergence

is observed. In practice, this is achieved by having the flux-tube undergo multiple poloidal turns before it connects back onto itself, *i.e.* by increasing  $L_z = N_{pol} \cdot 2\pi$  with  $N_{pol} > 1$ , instead of  $L_z = 2\pi$  usually considered. Given that self-interaction is a result of microinstability eigenmodes ‘biting their tails’ after one poloidal turn at corresponding MRSs, this approach weakens the self-interaction mechanism.

**Acknowledgements:** The authors would like to thank F. Jenko, T. Görler and D. Told for useful discussions pertaining to this work. This work has been carried out within the framework of the EUROfusion Consortium and has received funding from the Euratom research and training programme 2014-2018 and 2019-2020 under grant agreement no. 633053. The views and opinions expressed herein do not necessarily reflect those of the European Commission. We acknowledge the CINECA award under the ISCRA initiative, for the availability of high performance computing resources and support. Lastly, this work was supported by a grant from the Swiss National Supercomputing Centre(CSCS) under project ID s863 and s956.

## REFERENCES

- ABITEBOUL, J. 2012 Turbulent and neoclassical toroidal momentum transport in tokamak plasmas. PhD thesis, Aix-Marseille Université.
- ABITEBOUL, J., GARBET, X., GRANDGIRARD, V., ALLFREY, S. J., GHENDRIH, PH., LATU, G., SARAZIN, Y. & STRUGAREK, A. 2011 Conservation equations and calculation of mean flows in gyrokinetics. *Physics of Plasmas* **18** (8), 082503.
- BALL, J., BRUNNER, S. & C.J., AJAY 2020 Eliminating turbulent self-interaction through the parallel boundary condition in local gyrokinetic simulations. *Journal of Plasma Physics* **86** (2), 905860207.
- BEER, M. A., COWLEY, S. C. & HAMMETT, G. W. 1995 Field-aligned coordinates for nonlinear simulations of tokamak turbulence. *Physics of Plasmas* **2** (7), 2687–2700.
- BIGLARI, H., DIAMOND, P. H. & TERRY, P. W. 1990 Influence of sheared poloidal rotation on edge turbulence. *Physics of Fluids B: Plasma Physics* **2** (1), 1–4.
- CANDY, J, BELLI, E A & STAEBLER, G 2020 Spectral treatment of gyrokinetic profile curvature. *Plasma Physics and Controlled Fusion* **62** (4), 042001.
- CHEN, LIU, LIN, ZHIHONG & WHITE, ROSCOE 2000 Excitation of zonal flow by drift waves in toroidal plasmas. *Physics of Plasmas* **7** (8), 3129–3132.
- CHOWDHURY, J., GANESH, R., ANGELINO, P., VACLAVIK, J., VILLARD, L. & BRUNNER, S. 2008 Role of non-adiabatic untrapped electrons in global electrostatic ion temperature gradient driven modes in a tokamak. *Physics of Plasmas* **15** (7), 072117.
- CONNOR, J. W., HASTIE, R. J. & TAYLOR, J. B. 1978 Shear, periodicity, and plasma ballooning modes. *Physical Review Letters* **40**, 396–399.
- DIAMOND, P. H., ITOH, S-I, ITOH, K. & HAHM, T. S. 2005 Zonal flows in plasma - a review. *Plasma Physics and Controlled Fusion* **47** (12A), R35.
- DIMITS, A. M., BATEMAN, G., BEER, M. A., COHEN, B. I., DORLAND, W., HAMMETT, G. W., KIM, C., KINSEY, J. E., KOTSCHENREUTHER, M., KRITZ, A. H., LAO, L. L., MANDREKAS, J., NEVINS, W. M., PARKER, S. E., REDD, A. J., SHUMAKER, D. E., SYDORA, R. & WEILAND, J. 2000 Comparisons and physics basis of tokamak transport models and turbulence simulations. *Physics of Plasmas* **7** (3), 969–983.
- DOMINSKI, J., BRUNNER, S., GÖRLER, T., JENKO, F., TOLD, D. & VILLARD, L. 2015 How non-adiabatic passing electron layers of linear microinstabilities affect turbulent transport. *Physics of Plasmas* **22** (6), 062303.
- DOMINSKI, J., McMILLAN, B. F., BRUNNER, S., MERLO, G., TRAN, T.-M. & VILLARD, L. 2017 An arbitrary wavelength solver for global gyrokinetic simulations. application to the study of fine radial structures on microturbulence due to non-adiabatic passing electron dynamics. *Physics of Plasmas* **24** (2), 022308.
- DORLAND, W., JENKO, F., KOTSCHENREUTHER, M. & ROGERS, B. N. 2000 Electron temperature gradient turbulence. *Physical Review Letters* **85**, 5579–5582.
- FABER, B. J., PUESCHEL, M. J., TERRY, P. W., HEGNA, C. C. & ROMAN, J. E. 2018 Stellarator microinstabilities and turbulence at low magnetic shear. *Journal of Plasma Physics* **84** (5), 905840503.
- FALCHETTO, G. L., VACLAVIK, J. & VILLARD, L. 2003 Global-gyrokinetic study of finite  $\beta$  effects on linear microinstabilities. *Physics of Plasmas* **10** (5), 1424–1436.
- GALLAGHER, S., HNAT, B., CONNAUGHTON, C., NAZARENKO, S. & ROWLANDS, G. 2012 The modulational instability in the extended Hasegawa-Mima equation with a finite larmor radius. *Physics of Plasmas* **19** (12), 122115.
- GÖRLER, T., LAPILLONNE, X., BRUNNER, S., DANNERT, T., JENKO, F., MERZ, F. & TOLD, D. 2011 The global version of the gyrokinetic turbulence code gene. *Journal of Computational Physics* **230** (18), 7053 – 7071.
- HAHM, T. S., BEER, M. A., LIN, Z., HAMMETT, G. W., LEE, W. W. & TANG, W. M. 1999 Shearing rate of time-dependent  $E \times B$  flow. *Physics of Plasmas* **6** (2-3), 922–926.
- HALLATSCHEK, K. & DORLAND, W. 2005 Giant electron tails and passing electron pinch effects in tokamak-core turbulence. *Physical Review Letters* **95**, 055002.
- HASEGAWA, A., MACLENNAN, C. G. & KODAMA, Y. 1979 Nonlinear behavior and turbulence spectra of drift waves and rossby waves. *The Physics of Fluids* **22** (11), 2122–2129.
- HASEGAWA, A. & MIMA, K. 1978 Pseudo-three-dimensional turbulence in magnetized nonuniform plasma. *The Physics of Fluids* **21** (1), 87–92.

- HATCH, D. R., TERRY, P. W., JENKO, F., MERZ, F. & NEVINS, W. M. 2011 Saturation of gyrokinetic turbulence through damped eigenmodes. *Physical Review Letters* **106**, 115003.
- HAZELTINE, R. D. & NEWCOMB, W. A. 1990 Inversion of the ballooning transformation. *Physics of Fluids B: Plasma Physics* **2** (1), 7–10.
- HORTON, W. 1999 Drift waves and transport. *Reviews of Modern Physics* **71**, 735–778.
- JENKO, F., DORLAND, W., KOTSCHENREUTHER, M. & ROGERS, B. N. 2000 Electron temperature gradient driven turbulence. *Physics of Plasmas* **7** (5), 1904–1910.
- KROMMES, JOHN A. & KIM, CHANG-BAE 2000 Interactions of disparate scales in drift-wave turbulence. *Physical Review E* **62**, 8508–8539.
- LAPILLONNE, X., BRUNNER, S., DANNERT, T., JOLLIET, S., MARINONI, A., VILLARD, L., GORLER, T., JENKO, F. & MERZ, F. 2009 Clarifications to the limitations of the s-alpha equilibrium model for gyrokinetic computations of turbulence. *Physics of Plasmas* **16** (3), 032308.
- LIN, Z., HAHM, T. S., LEE, W. W., TANG, W. M. & WHITE, R. B. 1998 Turbulent transport reduction by zonal flows: Massively parallel simulations. *Science* **281** (5384), 1835–1837.
- McMILLAN, B., LAPILLONNE, X., BRUNNER, S., VILLARD, L., JOLLIET, S., BOTTINO, A., GOERLER, T. & JENKO, F. 2010 System size effects on gyrokinetic turbulence. *Physical Review Letters* **105**, 155001.
- MERZ, F. 2008 Gyrokinetic simulation of multimode plasma turbulence. PhD thesis, Universität Münster.
- PARRA, FELIX I & CATTO, PETER J 2009 Vorticity and intrinsic ambipolarity in turbulent tokamaks. *Plasma Physics and Controlled Fusion* **51** (9), 095008.
- ROSENBLUTH, M. N. & HINTON, F. L. 1998 Poloidal flow driven by ion-temperature-gradient turbulence in tokamaks. *Physical Review Letters* **80**, 724–727.
- SCOTT, B. 1998 Global consistency for thin flux tube treatments of toroidal geometry. *Physics of Plasmas* **5** (6), 2334–2339.
- WALTZ, R. E. 2005 Rho-star scaling and physically realistic gyrokinetic simulations of transport in diii-d. *Fusion Science and Technology* **48** (2), 1051–1059.
- WALTZ, R. E., AUSTIN, M. E., BURRELL, K. H. & CANDY, J. 2006 Gyrokinetic simulations of off-axis minimum-q profile corrugations. *Physics of Plasmas* **13** (5), 052301.
- WALTZ, R. E., CANDY, J. M. & ROSENBLUTH, M. N. 2002 Gyrokinetic turbulence simulation of profile shear stabilization and broken gyrobohm scaling. *Physics of Plasmas* **9** (5), 1938–1946.
- WALTZ, R. E., DEWAR, R. L. & GARBET, X. 1998 Theory and simulation of rotational shear stabilization of turbulence. *Physics of Plasmas* **5** (5), 1784–1792.
- WALTZ, R. E., KERBEL, G. D. & MILOVICH, J. 1994 Toroidal gyro-landau fluid model turbulence simulations in a nonlinear ballooning mode representation with radial modes. *Physics of Plasmas* **1** (7), 2229–2244.
- WEIKL, A., PEETERS, A. G., RATH, F., SEIFERLING, F., BUCHHOLZ, R., GROSSHAUSER, S. R. & STRINTZI, D. 2018 The occurrence of staircases in ITG turbulence with kinetic electrons and the zonal flow drive through self-interaction. *Physics of Plasmas* **25** (7), 072305.